Detector Blur and Correlated Noise Modeling for Digital Breast Tomosynthesis Reconstruction

Jiabei Zheng, *Member, IEEE*, Jeffrey A. Fessler, *Fellow, IEEE*, and Heang-Ping Chan

Abstract— This paper describes a new image reconstruction method for digital breast tomosynthesis (DBT). The new method incorporates detector blur into the forward model. The detector blur in DBT causes correlation in the measurement noise. By making a few approximations that are reasonable for breast imaging, we formulated a regularized quadratic optimization problem with a data-fit term that incorporates models for detector blur and correlated noise (DBCN). We derived a computationally efficient separable quadratic surrogate (SQS) algorithm to solve the optimization problem that has a non-diagonal noise covariance matrix. We evaluated the SQS-DBCN method by reconstructing DBT scans of breast phantoms and human subjects. The contrast-to-noise ratio and sharpness of microcalcifications were analyzed and compared with those by the simultaneous algebraic reconstruction technique. The quality of soft tissue lesions and parenchymal patterns was examined. The results demonstrate the potential to improve the image quality of reconstructed DBT images by incorporating the system physics model. This paper is a first step toward model-based iterative reconstruction for DBT.

Index Terms— Digital breast tomosynthesis, detector blur, correlated noise, model-based iterative reconstruction.

I. Introduction

DIGITAL breast tomosynthesis (DBT) has been developed to reduce the problem of overlapping tissue in conventional two-dimensional mammography [1]–[3]. In DBT, the commonly used reconstruction method is filtered back projection (FBP) [4]–[9]. Studies have demonstrated the promise of iterative reconstruction (IR) methods in DBT [2], [10]–[15]. Among commercial DBT systems, Hologic and Siemens use FBP and General Electric (GE) uses an adaptive statistical iterative reconstruction (ASIR). Among the IR methods, model-based iterative reconstruction (MBIR) methods incorporate the physics model of the system and the statistical model of signal detection. MBIR methods have been investigated extensively in CT and superior image quality has been observed [16]–[20].

However, existing MBIR methods for CT do not consider noise correlation/aliasing and detector blur because clinical CT systems use individual detector elements. Modeling detector blur and correlated noise was attempted only recently in cone-beam CT (CBCT) using flat-panel detectors [21]–[23]. For DBT, although some studies on MBIR methods have been conducted [24], [25], they considered only limited aspects of the system model, such as modeling the scattered radiation or the statistical model of the measurement noise. To our knowledge, no studies have incorporated the models of image degradation factors of the DBT imaging system, including the crosstalk of the flat-panel detector and the resulting noise correlation. Our goal is to develop MBIR methods with more comprehensive modeling of the system physics and computationally efficient algorithms for DBT reconstruction.

In a DBT system using an indirect detector, light diffusion in the phosphor or the scintillator introduces crosstalk between neighboring pixels. The finite pixel size and light diffusion contribute to blurring of the measured image and correlation in noise. Neglecting detector blur leads to blurring of the reconstructed objects, strongly affecting small features such as microcalcifications (MC). In CT applications, several projectors have been proposed that account for the finite pixel size, such as the distance-driven projector [26] and the separable footprint projector [27]. We have proposed a segmented separable projector (SG projector) for DBT geometries [28]. Current DBT reconstruction algorithms generally treat the measurement at each detector element to be independent random variables, which differs from the physical process in the DBT detector. Tilley et al. and Stayman et al. studied the effect of modeling the detector blur and correlated noise in least-squares reconstruction for CBCT with simulated phantoms and found superior noise-resolution trade-offs with their proposed approach [21]–[23]. Our feasibility study [29] showed similar promise for DBT scans. In this paper, we further refine our implementation of DBT reconstruction accounting for detector blur and the resulting noise correlation, incorporate adaptive regularization strength, analyze the image quality by the contrast and sharpness of the signals and the tissue texture using phantom and human subject DBT scans, and compare the reconstructed image quality with and without modeling detector blur and noise correlation.

DBT is a limited-angle x-ray tomography technique using low-dose high-resolution projections. It is an ill-posed problem with sparse projection view (PV) sampling. As a result, small measurement fluctuation such as noise could cause large perturbations of the reconstructed images in the absence of suitable regularization. On the other hand, the PVs of DBT are

noisy by nature since the total x-ray dose of all PVs is kept to be about the same as that of a mammogram. Regularization is therefore crucial for iterative reconstruction algorithms to prevent noise amplification and maintain consistency. Several studies have been conducted on regularization of limited-angle reconstruction. For example, the total variation (TV) method was applied to tomographic reconstruction [11], [30]. Selective diffusion regularization was proposed to enhance MCs while reducing noise [31]. Other regularization methods used the bilateral filter [32], [33]. In this paper, we use a regularization strategy based on a hyperbola potential function, which is convex and edge-preserving. We model detector blur and noise correlation and formulate the reconstruction as a regularized quadratic optimization problem. The problem needs to be solved with an iterative algorithm. Based on the form of the data-fit term and the regularization, we chose to apply a slightly modified separable quadratic surrogate (SQS) [34] method. Although the SQS method requires more iterations to converge than coordinate descent methods, it enforces non-negativity constraints on the reconstructed image [35], [36].

Section II introduces our detector blur model and the assumptions used for its simplification. We describe the optimization problem and the cost function for regularized reconstruction. Section III introduces the geometry of our DBT system and the figures of merit used for quantitative comparisons of image quality. Results in Section IV demonstrate the usefulness of the method by comparing its reconstructed image quality with that by simultaneous algebraic reconstruction technique (SART) using DBT of both breast phantom and human subjects. We also compare the images reconstructed by modeling both detector blur and noise correlation to those without modeling either component to study their impact on the image quality. Section V discusses the potential of MBIR for improving DBT image quality and future work.

II. METHODS

A. Formulation of the Reconstruction Problem

We first mathematically formulate the reconstruction problem using a few assumptions based on the imaging characteristics of DBT. Let $\mathbf{A}_i$ denote the $N \times M$ projector matrix for the ith projection angle, for $i = 1, \ldots, N_\mathrm{p}$, where N_p denotes the number of PV angles. Let N denote the number of pixels in a DBT projection image and M the number of object voxels to be reconstructed. Let $\mathbf{f}$ denote the length-M vector corresponding to the unknown array of attenuation coefficients in the imaged volume and $\mathbf{Y}_i$ the length-N vector corresponding to the measured PV image at the ith projection angle. Considering the detector blur and the Lambert-Beer law for attenuation, a reasonable model for the expectation $\bar{\mathbf{Y}}_i$ is [22]:

$$\bar{\mathbf{Y}}_i = I_0 \mathbf{B}_i \exp(-\mathbf{A}_i \mathbf{f}), \tag{1}$$

where $\mathbf{B}_i$ denotes the blurring operation in $N \times N$ matrix form and I_0 is the constant expected projection value if there is no object present in the imaged volume, assuming there is no non-uniformity due to Heel effect or cone-beam geometry. In this work, we assume that $\mathbf{B}_i$ is projection-angle-dependent

but linear shift-invariant within a given projection. Focal spot blur is ignored in the current study. If the incident intensity I_0 is nonuniform over the PV then one could replace the scale I_0 with a diagonal matrix.

One challenge in performing image reconstruction with the model in (1) is that the matrix $\mathbf{B}_i$ before the exponential is not diagonal [21]–[23]. To address this challenge for DBT, we assume that the image $\mathbf{f}$ consists of two parts ($\mathbf{f} = \mathbf{f}_\mathrm{b} + \mathbf{f}_\mathrm{s}$), where $\mathbf{f}_\mathrm{b}$ is a low-frequency background whose projections are approximately uniform within the support of the blurring kernel ($\mathbf{B}_i \mathbf{A}_i \mathbf{f}_\mathrm{b} \approx \mathbf{A}_i \mathbf{f}_\mathrm{b}$), and $\mathbf{f}_\mathrm{s}$ is a small structure such as MC in DBT whose attenuation contributes only a small amount to the projection values ($\mathbf{A}_i \mathbf{f}_\mathrm{s} \ll 1$). These assumptions are more reasonable in breast imaging than in CT of body parts that include bone or other high-attenuation objects. Under these assumptions, we use the following approximation:

$$
\begin{aligned}
\mathbf{B}_i \exp\left(-\mathbf{A}_i \mathbf{f}\right) &= \mathbf{B}_i \exp\left(-\mathbf{A}_i \mathbf{f}_\mathrm{s}\right) \exp\left(-\mathbf{A}_i \mathbf{f}_\mathrm{b}\right) \\
&\approx \mathbf{B}_i \left(1 - \mathbf{A}_i \mathbf{f}_\mathrm{s}\right) \exp\left(-\mathbf{B}_i \mathbf{A}_i \mathbf{f}_\mathrm{b}\right) \\
&= \left(1 - \mathbf{B}_i \mathbf{A}_i \mathbf{f}_\mathrm{s}\right) \exp\left(-\mathbf{B}_i \mathbf{A}_i \mathbf{f}_\mathrm{b}\right) \\
&\approx \exp\left(-\mathbf{B}_i \mathbf{A}_i \mathbf{f}_\mathrm{s}\right) \exp\left(-\mathbf{B}_i \mathbf{A}_i \mathbf{f}_\mathrm{b}\right) \\
&= \exp\left(-\mathbf{B}_i \mathbf{A}_i \mathbf{f}\right). \tag{2}
\end{aligned}
$$

Then we have the following simplification of (1) for DBT:

$$\bar{\mathbf{Y}}_i \approx I_0 \exp(-\mathbf{B}_i \mathbf{A}_i \mathbf{f}). \tag{3}$$

The expectation $\bar{\mathbf{y}}_i$ of the log-transformed projection $\mathbf{y}_i$ is approximately:

$$\bar{\mathbf{y}}_i = \log(I_0/\mathbf{Y}_i) = \mathbf{B}_i \mathbf{A}_i \mathbf{f}. \tag{4}$$

Compared with the reconstruction problem without detector blur, we simply need to include a blurring operation in the forward projection step. The transpose of $\mathbf{B}_i$ is also relatively easy to implement in the back-projection step needed for iterative image reconstruction.

The cost function of the reconstruction problem should also account for the covariance matrix of the noise in the measurements $\mathbf{y}_i$. DBT systems usually use a flat-panel direct or indirect detector. In our model, we assume an indirect CsI phosphor/a:Si active matrix flat panel detector. The image noise contains two major components: quantum noise from the x-ray photons and electronic noise of the detector. The quantum noise in the imaging process is affected by the detector blur but the detector electronic noise is not.

Accounting for both quantum and electronic noise, we follow [22] and use the following model for the noise covariance $\mathbf{K}_i$ of the ith projection view:

$$\mathbf{K}_i = \mathbf{B}_i \mathbf{K}_i^\mathrm{q} \mathbf{B}_i' + \mathbf{K}_i^\mathrm{r}, \tag{5}$$

where $'$ denotes the transpose of a matrix. $\mathbf{K}_i^\mathrm{q}$ and $\mathbf{K}_i^\mathrm{r}$ denote diagonal matrices with elements corresponding to the variances of quantum noise and readout noise at each detector element, respectively. Section VII of the Supplementary Material shows the detailed derivation of (5).

Assuming $\mathbf{y}_i$ follows approximately a Gaussian distribution, $\mathbf{y}_i \sim N\left(\bar{\mathbf{y}}_i, \mathbf{K}_i\right)$, we formulate for DBT the following

regularized image reconstruction problem with non-diagonal weighting:

$$\hat{\mathbf{f}} = \underset{\mathbf{f}}{\arg\min} \frac{1}{2} \sum_{i=1}^{N_p} \left\| \mathbf{y}_i - \mathbf{B}_i \mathbf{A}_i \mathbf{f} \right\|^2_{(\mathbf{B}_i \mathbf{K}_i^q \mathbf{B}_i' + \mathbf{K}_i^r)^{-1}} + R(\mathbf{f})$$

$$= \underset{\mathbf{f}}{\arg\min} \frac{1}{2} \sum_{i=1}^{N_p} \left\| \mathbf{S}_i \mathbf{y}_i - \mathbf{S}_i \mathbf{B}_i \mathbf{A}_i \mathbf{f} \right\|^2_2 + R(\mathbf{f}), \quad (6)$$

where $R(\mathbf{f})$ denotes the regularization term and the inverse matrix square root of the noise covariance is

$$\mathbf{S}_i = (\mathbf{B}_i \mathbf{K}_i^q \mathbf{B}_i' + \mathbf{K}_i^r)^{-1/2}. \quad (7)$$

B. Implementing $\mathbf{S}_i$

Since $(\mathbf{B}_i \mathbf{K}_i^q \mathbf{B}_i' + \mathbf{K}_i^r)$ is non-diagonal, implementing multiplication by $\mathbf{S}_i$ is usually very challenging, and this is the key difficulty in using the optimization formulation (6). In CT applications, one possible method is to solve another inner optimization problem with a set of conjugate gradient iterations [22]. In DBT, we can dramatically simplify the implementation by making some reasonable assumptions. Unlike body CT where there exist large bones and even perhaps metal objects of significant size that are strongly attenuating, the compressed breast has a fairly consistent thickness mainly composed of soft tissue. As a first-order approximation, we treat quantum noise variance as constant across all detector elements in a given projection angle:

$$\mathbf{K}_i^q = \sigma_i^{q2} \mathbf{I}, \quad (8)$$

where $\mathbf{I}$ denotes the $N \times N$ identity matrix. Sections VIII and IX of the Supplementary Material describe the justification of this approximation. In addition, we treat all detector elements in a given projection view as having similar readout noise variance:

$$\mathbf{K}_i^r = \sigma_i^{r2} \mathbf{I}. \quad (9)$$

Let $\mathbf{h}_i$ denote the point spread function of the detector. We obtained $\mathbf{h}_i$ by the inverse Fourier transform of the modulation transfer function (MTF) of the detector for a GE Essential mammography system [37], which also agreed with our own measurement on the prototype DBT system using the edge method [38]. We diagonalize the blurring operation by $\mathbf{B}_i = \mathbf{Q}^{-1} \mathbf{H}_i \mathbf{Q}$, where $\mathbf{Q}$ denotes the discrete Fourier transform (DFT) matrix, and $\mathbf{H}_i = \text{Diag}(\text{DFT}\{\mathbf{h}\}_i)$ denotes the corresponding frequency response. We then implement the operation of multiplying $\mathbf{S}_i$ by a vector using FFT operations without needing any iterative method for matrix inversion:

$$\mathbf{S}_i = \mathbf{Q}^{-1} (\sigma_i^{q2} \mathbf{H}_i \mathbf{H}_i' + \sigma_i^{r2} \mathbf{I})^{-1/2} \mathbf{Q}, \quad (10)$$

where σ_i^q and σ_i^r with lower case superscripts q and r denote noise standard deviations for the PVs after log transform, or equivalently the noise level relative to the recorded x-ray intensity. The corresponding noise standard deviations before log transform are denoted by σ_i^Q and σ_i^R with upper case superscripts Q and R. We estimate σ_i^R from dark current images without x-ray exposure by subtracting two dark current images to remove possible structured noise from the detector, then calculating a mean standard deviation σ_i^R from noise

patches on the subtracted image and dividing it by $\sqrt{2}$. The breast boundary is automatically detected on each PV [39]. We then estimate the mean x-ray intensity $\bar{Y}_i$ incident on the detector as the mean pixel value within the breast boundary and calculate σ_i^r as the ratio of σ_i^R over $\bar{Y}_i$.

Estimating σ_i^q is more complicated since it is difficult to remove the heterogeneous tissue background from the projection images. Therefore, we use a DBT scan of a uniform Lucite slab of approximately the thickness of the phantom or a breast to estimate σ_i^q. For each PV of the Lucite slab, we select an array of noise patches and remove the background trend with a 2-D second order polynomial fitting. Then we calculate the standard deviation σ_i as the mean of the standard deviations estimated from each noise patch. This calculated σ_i contains the contribution of both σ_i^R and σ_i^Q as given by:

$$\sigma_i^2 = \sigma_i^{Q2} \|\mathbf{h}_i\|_2^2 + \sigma_i^{R2}. \quad (11)$$

We then derive σ_i^Q of the Lucite slab from the above relationship using the estimated σ_i and σ_i^R:

$$\sigma_i^Q = \sqrt{\frac{\sigma_i^2 - \sigma_i^{R2}}{\|\mathbf{h}_i\|_2^2}}. \quad (12)$$

Treating σ_i^Q as approximately Poisson noise, σ_i^{Q2} is proportional to $\bar{Y}_i$ and therefore σ_i^{q2} is inversely proportional to $\bar{Y}_i$. Using the ratio of $\bar{Y}_i$ between a DBT scan and the Lucite slab, we estimate σ_i^q for the DBT scan to be reconstructed. In practical implementation, this may be accomplished by predetermining sets of σ_i^Q ($i = 1, \ldots, N_p$) for all N_p projections from Lucite slabs over a range of thicknesses and x-ray spectra (anode, filter, kilovoltage) combinations and storing them as a library of look up values. For a given DBT scan acquired with a certain exposure technique, one can select an appropriate set that approximates the breast thickness and exposure technique for reconstruction.

C. Regularization

In the implementation of (7), $\mathbf{S}_i$ acts as a filter that boosts high spatial frequencies. The typical frequency response of $\mathbf{S}_i$ is shown in Section X of the Supplementary Material. $\mathbf{S}_i$ would amplify noise in reconstruction if used without regularization. Regularization is important for stable reconstruction. We use a regularization term of the following form:

$$R(\mathbf{f}) = \frac{\alpha\beta}{1+\gamma} \left(\sum_j \eta\left([\mathbf{C}_x \mathbf{f}]_j\right) + \eta\left([\mathbf{C}_y \mathbf{f}]_j\right) \right.$$
$$\left. + \gamma\, \eta\left([\mathbf{C}_{x-y} \mathbf{f}]_j\right) + \gamma\, \eta\left([\mathbf{C}_{x+y} \mathbf{f}]_j\right) \right), \quad (13)$$

where $\mathbf{C}_x$ and $\mathbf{C}_y$ denote matrices that calculate differences between neighboring pixels along the x and y-direction, respectively, as defined in Fig. 1. $\mathbf{C}_{x-y}$ and $\mathbf{C}_{x+y}$ compute finite differences along the two diagonal directions. j is the index for all neighboring pixel pairs along one direction. The distance between two neighboring pixels along the diagonal direction is larger, resulting in relatively weaker correlation between their pixel values. We therefore use the parameter γ ($\gamma \leq 1$) to control the weight of regularization in the
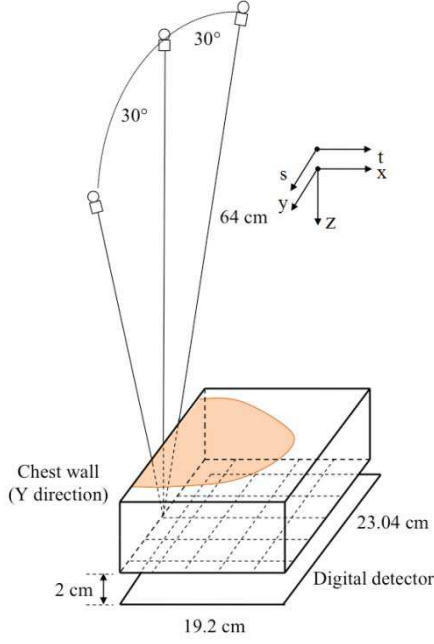
Fig. 1. Geometry of the DBT system used in this study.

diagonal directions. We chose γ to be 0.5 for this study following [40]. The parameter β controls the strength of the regularization term. From reconstructing DBT at different noise levels, we observed that the regularization parameter needs to be adapted to keep an appropriate balance between the data-fit term and the regularizer, because the covariance-based weighting of the data-fit term in (6) depends on the noise level. Therefore we include a scaling factor α to adaptively adjust the regularization strength based on the noise level of the projections. We define α as:

$$\alpha = \frac{N_{\mathrm{p}}}{\sum_{i=1}^{N_{\mathrm{p}}} \sigma_i^{\mathrm{q}2} \|\mathbf{h}_i\|_2^2 + \sigma_i^{\mathrm{r}2}}. \tag{14}$$

For the regularizer (13), we use a hyperbola potential function $\eta(t)$:

$$\eta(t) = \delta^2 \left(\sqrt{1 + (t/\delta)^2} - 1 \right). \tag{15}$$

This form of $\eta(t)$ is edge-preserving. $\eta(t)$ is also differentiable, making it easy to implement the optimization algorithm of the cost function. The parameters δ and β need to be chosen properly as discussed in Section IV.A. When δ is large relative to t, (15) is approximately $\eta(t) = t^2$, which is equivalent to a quadratic regularization.

D. The Reconstruction Algorithm

Both the quadratic function of the data-fit term and $\eta(t)$ are convex and the second-order derivative of $\eta(t)$ in (15) is

$$\ddot{\eta}(t) = \left(1 + \left(\frac{t}{\delta} \right)^2 \right)^{-3/2}, \tag{16}$$

which is less than or equal to 1, enabling the use of the SQS algorithm to solve the optimization problem [35]. To apply

the SQS algorithm, we need to find an upper bound on the Hessian of the cost function

$$\Psi(\mathbf{f}) = \frac{1}{2} \left\| \tilde{\mathbf{y}} - \tilde{\mathbf{A}}\mathbf{f} \right\|_2^2 + R(\mathbf{f}), \tag{17}$$

where the whole system matrix and whole (prewhitened) data vector are given by:

$$\tilde{\mathbf{A}} = \begin{pmatrix} \tilde{\mathbf{A}}_1 \\ \vdots \\ \tilde{\mathbf{A}}_{N_{\mathrm{p}}} \end{pmatrix} = \begin{pmatrix} \mathbf{S}_1 \mathbf{B}_1 \mathbf{A}_1 \\ \vdots \\ \mathbf{S}_{N_{\mathrm{p}}} \mathbf{B}_{N_{\mathrm{p}}} \mathbf{A}_{N_{\mathrm{p}}} \end{pmatrix}, \tag{18}$$

$$\tilde{\mathbf{y}} = \begin{pmatrix} \tilde{\mathbf{y}}_1 \\ \vdots \\ \tilde{\mathbf{y}}_{N_{\mathrm{p}}} \end{pmatrix} = \begin{pmatrix} \mathbf{S}_1 \mathbf{y}_1 \\ \vdots \\ \mathbf{S}_{N_{\mathrm{p}}} \mathbf{y}_{N_{\mathrm{p}}} \end{pmatrix}. \tag{19}$$

We first find an upper bound on the Hessian of the regularization term $R(\mathbf{f})$. Since the second-order derivative of the potential function $\eta(t)$ is less than or equal to 1, we have

$$\nabla^2 \sum_j \eta \left([\mathbf{Cf}]_j \right) \leq \mathrm{diag}\left\{ |\mathbf{C}'| |\mathbf{C}| \mathbf{1} \right\} = 4\mathbf{I}, \tag{20}$$

where $\mathbf{1}$ denotes a length-M all-one vector, $|\cdot|$ denotes element-wise absolute value, $\mathbf{I}$ denotes the identity matrix and $\mathbf{C}$ denotes any one of $\mathbf{C}_x$, $\mathbf{C}_y$, $\mathbf{C}_{x+y}$ and $\mathbf{C}_{x-y}$. As a result, we have:

$$\nabla^2 R(\mathbf{f}) \leq \frac{\alpha\beta}{1+\gamma} (4 + 4 + 4\gamma + 4\gamma) \mathbf{I} = 8\alpha\beta\mathbf{I}. \tag{21}$$

By finding (below) a diagonal majorizing matrix $\mathbf{D}$ such that $\mathbf{D} \geq |\tilde{\mathbf{A}}'||\tilde{\mathbf{A}}|$, the modified SQS algorithm for minimizing the DBT cost function is (with nonnegativity constraint):

$$\mathbf{f}^{(n+1)} = \max\left(\mathbf{f}^{(n)} - (\mathbf{D} + 8\alpha\beta\mathbf{I})^{-1} \nabla\Psi\left(\mathbf{f}^{(n)}\right), 0 \right). \tag{22}$$

The usual choice of $\mathbf{D}$ would be $\mathbf{D} = \mathrm{diag}\left\{ |\tilde{\mathbf{A}}'||\tilde{\mathbf{A}}|\mathbf{1} \right\}$. However, implementing $|\tilde{\mathbf{A}}'||\tilde{\mathbf{A}}|\mathbf{1}$ is difficult since $\tilde{\mathbf{A}}$ has negative values because of the high-frequency boosting feature of $\mathbf{S}_i$. Instead, note that the blur frequency response matrix $\mathbf{H}_i$ satisfies $\mathbf{H}_i \mathbf{H}_i' \leq \mathbf{I}$, then we have from (10):

$$\mathbf{B}_i' \mathbf{S}_i' \mathbf{S}_i \mathbf{B}_i = \mathbf{Q}^{-1} \mathbf{H}_i' \left(\sigma_i^{\mathrm{q}2} \mathbf{H}_i \mathbf{H}_i' + \sigma_i^{\mathrm{r}2} \mathbf{I} \right)^{-1} \mathbf{H}_i \mathbf{Q}$$
$$\leq \mathbf{Q}^{-1} \left(\left(\sigma_i^{\mathrm{q}2} + \sigma_i^{\mathrm{r}2} \right)^{-1} \mathbf{I} \right) \mathbf{Q} = \left(\sigma_i^{\mathrm{q}2} + \sigma_i^{\mathrm{r}2} \right)^{-1} \mathbf{I}. \tag{23}$$

This inequality leads to the following diagonal majorizer:

$$\tilde{\mathbf{A}}' \tilde{\mathbf{A}} = \sum_{i=1}^{N_{\mathrm{p}}} \mathbf{A}_i' \mathbf{B}_i' \mathbf{S}_i' \mathbf{S}_i \mathbf{B}_i \mathbf{A}_i$$
$$\leq \sum_{i=1}^{N_{\mathrm{p}}} \left(\sigma_i^{\mathrm{q}2} + \sigma_i^{\mathrm{r}2} \right)^{-1} \mathbf{A}_i' \mathbf{A}_i \leq \mathbf{D}, \tag{24}$$

where

$$\mathbf{D} = \sum_{i=1}^{N_{\mathrm{p}}} \left(\sigma_i^{\mathrm{q}2} + \sigma_i^{\mathrm{r}2} \right)^{-1} \mathrm{diag}\left\{ \mathbf{A}_i' \mathbf{A}_i \mathbf{1} \right\} \tag{25}$$

This diagonal majorizer is as easy to implement as the usual SQS majorizer [34].

In iterative DBT reconstruction, usually only one projection view is used at a time to update the image. We use the ordered

subset (OS) approximation [34] to further accelerate the SQS reconstruction:

$$\nabla \sum_{i=1}^{N_\mathrm{p}} \left\| \tilde{\mathbf{y}}_i - \tilde{\mathbf{A}}_i \mathbf{f} \right\|_2^2 \approx N_\mathrm{p} \nabla \left(\left\| \tilde{\mathbf{y}}_i - \tilde{\mathbf{A}}_i \mathbf{f} \right\|_2^2 \right). \quad (26)$$

The OS reconstruction update is given by:

$$\mathbf{f}^{(n,i+1)} = \mathbf{f}^{(n,i)} - (\mathbf{D} + 8\alpha\beta\mathbf{I})^{-1} \nabla\Psi_i \left(\mathbf{f}^{(n,i)} \right), \quad (27)$$

$$\nabla\Psi_i \left(\mathbf{f}^{(n,i)} \right) = \nabla R \left(\mathbf{f}^{(n,i)} \right) + N_\mathrm{p} \tilde{\mathbf{A}}_i' \left(\tilde{\mathbf{A}}_i \mathbf{f}^{(n,i)} - \tilde{\mathbf{y}}_i \right), \quad (28)$$

$$\nabla R(\mathbf{f}^{(n,i)}) = \frac{\alpha\beta}{1+\gamma} \Big(\mathbf{C}_x' \dot{\eta}(\mathbf{C}_x \mathbf{f}^{(n,i)}) + \mathbf{C}_y' \dot{\eta}(\mathbf{C}_y \mathbf{f}^{(n,i)})$$
$$+ \gamma \, \mathbf{C}_{x-y}' \dot{\eta}(\mathbf{C}_{x-y} \mathbf{f}^{(n,i)})$$
$$+ \gamma \, \mathbf{C}_{x+y}' \dot{\eta}(\mathbf{C}_{x+y} \mathbf{f}^{(n,i)}) \Big). \quad (29)$$

The iteration counter n is incremented by 1 after all measured projections have been used once.

The OS approximation used in the reconstruction makes the method somewhat similar to SART, where also one projection is used in each update, and facilitates their comparison. The OS algorithm was proposed for PET and CT reconstruction [41] where the subsets are better "balanced" than in DBT. For both CT and DBT, the standard OS–SQS algorithm is not guaranteed to converge. The OS algorithm could be made convergent by some relaxation [42], which has not been implemented in this study.

We use SART as a reference algorithm in this paper; although not state-of-the-art, SART has been shown to provide good image quality for reconstructing DBT acquired with our prototype DBT system [10] and has been evaluated by other investigators [9], [43]. We implemented the SQS-DBCN reconstruction with the SG projector [28] and implemented SART with the ray-tracing projector [10], [44]. We previously compared the effects of ray-tracing and SF projectors to SG using SART in a phantom study [28], so here we focus on examining the new DBCN effects. Artifact reduction methods [45], [46] were implemented for all reconstruction methods in this study.

E. Reconstruction Without Detector Blur or Correlated Noise

We investigated the role of each model component in the SQS-DBCN method. The SQS-DBCN method includes the detector blur, the corresponding noise correlation and the regularization. To examine the effects of the detector blur and the noise correlation, we studied the following two reconstruction algorithms:

$$\hat{\mathbf{f}}_{\mathrm{noDB}} = \underset{\mathbf{f}}{\arg\min} \frac{1}{2} \sum_{i=1}^{N_\mathrm{p}} \left\| \mathbf{y}_i - \mathbf{A}_i \mathbf{f} \right\|_{(\mathbf{K}_i^\mathrm{q} + \mathbf{K}_i^\mathrm{r})^{-1}}^2 + R\left(\mathbf{f}\right), \quad (30)$$

$$\hat{\mathbf{f}}_{\mathrm{noNC}} = \underset{\mathbf{f}}{\arg\min} \frac{1}{2} \sum_{i=1}^{N_\mathrm{p}} \left\| \mathbf{y}_i - \mathbf{B}_i \mathbf{A}_i \mathbf{f} \right\|_{(\mathbf{K}_i^\mathrm{q} + \mathbf{K}_i^\mathrm{r})^{-1}}^2 + R\left(\mathbf{f}\right). \quad (31)$$

The no-detector-blur (noDB) reconstruction method neglects the detector blur by setting the point spread function to a Kronecker impulse such that $\mathbf{B}_i$ becomes an identity matrix. This is equivalent to a common approach to SQS

regularized reconstruction that ignores detector blur and noise correlation. For the no-noise-correlation (noNC) reconstruction, we kept the detector blur in the system model while neglecting the noise correlation caused by the detector blur to evaluate the effect of the correlated noise model in SQS-DBCN. We also studied the reconstruction with penalized weighted least-squares (PWLS) cost function [18], [36], which is equivalent to the SQS-noDB method with location-dependent noise variance. The results are very similar to those obtained with the SQS-noDB method as shown in Section IX of the Supplementary Material. Another case we investigated was keeping both the detector blur and noise correlation while neglecting the regularization. In this case, however, the reconstructed image became extremely noisy after only 2 or 3 SQS iterations, making it difficult even to recognize the reconstructed MCs. As a result, we omit the no-regularization results.

III. MATERIALS

A. DBT System

We used a GE GEN2 prototype DBT system for image acquisition in this study but the proposed method should be applicable to other DBT systems. Fig. 1 shows the imaging geometry. The system uses a CsI phosphor/a:Si active matrix flat panel detector with a pixel size of 0.1mm × 0.1mm and an area of 1920 × 2304 pixels. The detector is stationary during image acquisition. The distance from the x-ray source to the fulcrum at the breast support plate (bottom of the imaged volume) is 64 cm. There is a 2 cm gap between the fulcrum and the image plane of the detector. The reconstructed imaged volumes in this study had a rectangular voxel grid at a voxel size of 0.1mm × 0.1mm × 1 mm.

B. Breast Phantom and Human Subject DBT

MCs are small calcium deposits in the breast of sizes from about 0.1 mm to 0.5 mm. Clustered MCs and subtle masses are important signs of early breast cancer [47]. One of the main challenges in DBT reconstruction is to reduce noise while enhancing MCs and preserving the features of mass margins and the texture of the parenchyma. In this study, we used a breast phantom with embedded simulated MCs for evaluating reconstruction methods and parameter selection on the image quality of MCs. It is difficult to build mass phantoms with realistic spiculated or ill-defined margins that are strong indicators of breast cancer; we therefore used real breast DBT for visual evaluation of the image quality of masses. The human subject DBTs were previously acquired with approval of our Institutional Review Board and informed consent for a lesion detection project.

The breast phantom consists of a stack of five 1-cm-thick slabs of breast tissue mimicking material [48]. Eight clusters of calcium carbonate specks of nominal size range of 0.15-0.18 mm, eight clusters of 0.18-0.25 mm, and five clusters of 0.25-0.30 mm were sandwiched at random locations and depths between the slabs to simulate MCs of different conspicuity levels. For the human subject DBT, we selected cases with spiculated masses that were biopsy-proven to be invasive

ductal carcinomas. Both the phantom and human subject DBT were acquired with 60° scan angle, 3° increments and 21 projections. To simulate the DBT acquired with narrow-angle DBT system, we used the 9 central projections for reconstruction, corresponding 24° scan angle with 3° increments, which was close to the 25° scan angle and 3° increments for a GE commercial system. The x-ray exposure for each DBT was therefore reduced to less than half of the original values.

C. Figures of Merit (FOMs)

We use two FOMs for quantitative comparisons of reconstruction quality of MCs: contrast-to-noise ratio (CNR) and full-width at half maximum (FWHM). To calculate the FWHM of an MC on a reconstructed image, we apply a 2-D least-squares Gaussian fitting including a first-order background plane to a 13×13-pixel patch centered at the MC. With the fitted standard deviation σ_{MC}, the FWHM is given by $2.355\sigma_{MC}$. To calculate the CNR, we estimate the local noise level σ_{NP} as the root-mean-square noise in a 40×40-pixel noise patch near each cluster after subtracting a low-frequency background level estimated by a 2-D fitting with a second order polynomial to the patch. The CNR for an MC is calculated as $\mathrm{CNR} = A_{MC}/\sigma_{NP}$, where A_{MC} is the maximum value around the center of the fitted MC patch.

For MCs of a given nominal size range, a set of individual MCs were manually marked from the clusters at different locations and depths of the phantom, and the mean CNR and mean FWHM were calculated from the set to represent the CNR and FWHM of that MC size range. In total, we marked 30 MCs of 0.15-0.18 mm size, 48 MCs of 0.18-0.25 mm size and 44 MCs of 0.25-0.30 mm size for the analysis. The same set of MCs for each size range was used for the FOM calculation for all reconstruction techniques and parameters.

Although the SQS-DBCN reconstructed DBT is not a linear, shift-invariant system, we calculate an average noise power spectrum (NPS) of the heterogeneous phantom background to provide a comparison of the relative change in the global texture for the various reconstruction techniques and parameters. For each different reconstruction, we calculated the average NPS using sixty 200×200-pixel noise patches from 4 reconstructed slices at 4 different depths. We then took the radial average NPS for each reconstruction condition. The locations of the noise patches were chosen such that they did not contain any MC clusters and the same patch locations were used for all conditions. There is no FOM to reliably evaluate the fine details of the margin or spiculations of a cancerous lesion at present so that these features are compared visually on the reconstructed breast images.

IV. RESULTS

A. Effects of Regularization Parameters

The performance of the SQS-DBCN method depends on the parameters of the regularization term. We reconstructed the phantom DBT with different parameter combinations and plotted the corresponding CNR curves for the small-sized (0.15-0.18mm) and medium-sized (0.18-0.25mm) MCs, as shown in Fig. 2. These CNR curves
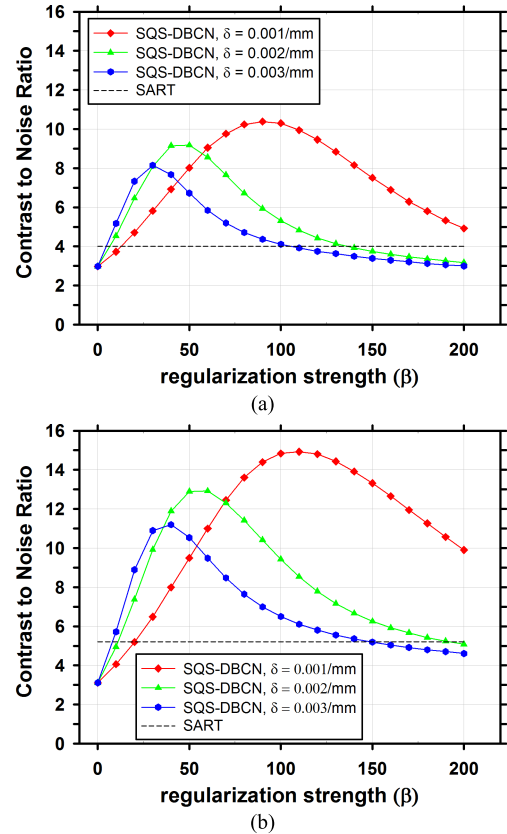

Fig. 2. Dependence of CNR on reconstruction parameters. The CNR is plotted as a function of β for a range of δ. The black dashed lines indicate the CNR level of the SART. (a) MCs of nominal size 0.15-0.18mm, (b) MCs of nominal size 0.18-0.25mm.

provide some guidance for parameter selection. The curves for the large-sized (0.25-0.30mm) MCs have similar trends but they are not shown because their CNRs are very high and the parameter settings are not expected to have a strong influence on their visibility. We did not show the FWHM curves either because they monotonically increase as β increases due to the increasing blurring effect of regularization, which is not useful for guiding parameter selection.

For the breast phantom, Fig. 3 shows the rotational average of the 2-D in-plane NPS for several sets of parameters. The pixel size of the slices is 0.1mm $\times$ 0.1mm, yielding a Nyquist frequency of 5 cycles/mm. As the parameters change, the middle and high frequency noise are mainly affected, while the low frequency noise almost stays the same. Fig. 3(c) shows the dependence of the NPS values on β at several frequencies. When weaker regularization is used ($\beta < 18$), the high-frequency NPS is higher than low-frequency NPS. On reconstructed images, the high level of high-frequency noise is superimposed with some salt-and-pepper noise, which is a very unfavorable visual feature. As the regularization strength is increased (larger β values), these noisy spikes become less and less noticeable.

For each MC size, there is a different 'optimal' parameter combination that yields maximum CNR. However, the parameter combination that yields the best CNR for MCs may generate artificially appearing texture for soft tissues or spurious noise in the background. Combining curves for both
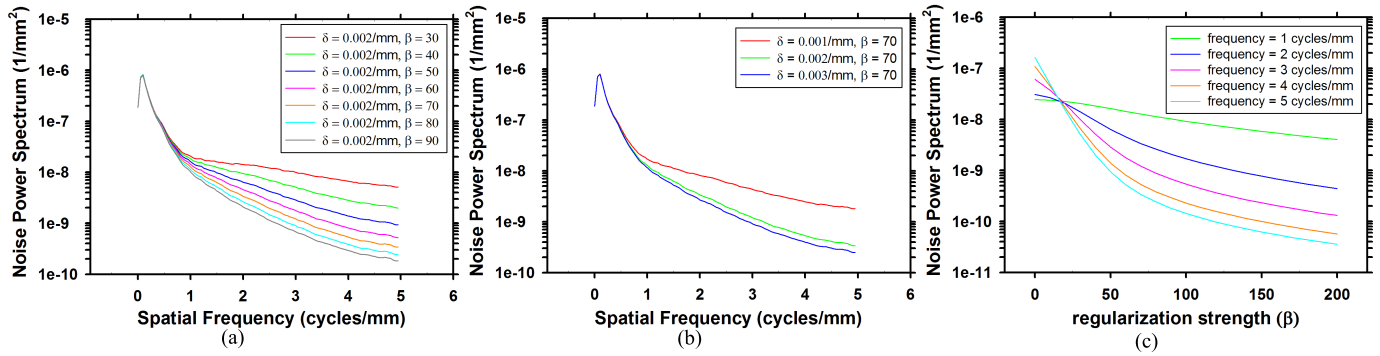
Fig. 3. Dependence of NPS on regularization parameters. (a) NPS with different β values at $\delta = 0.002$/mm. (b) NPS with different δ values at $\beta = 70$. (c) Dependence of noise power on β at five different frequencies at $\delta = 0.002$/mm.
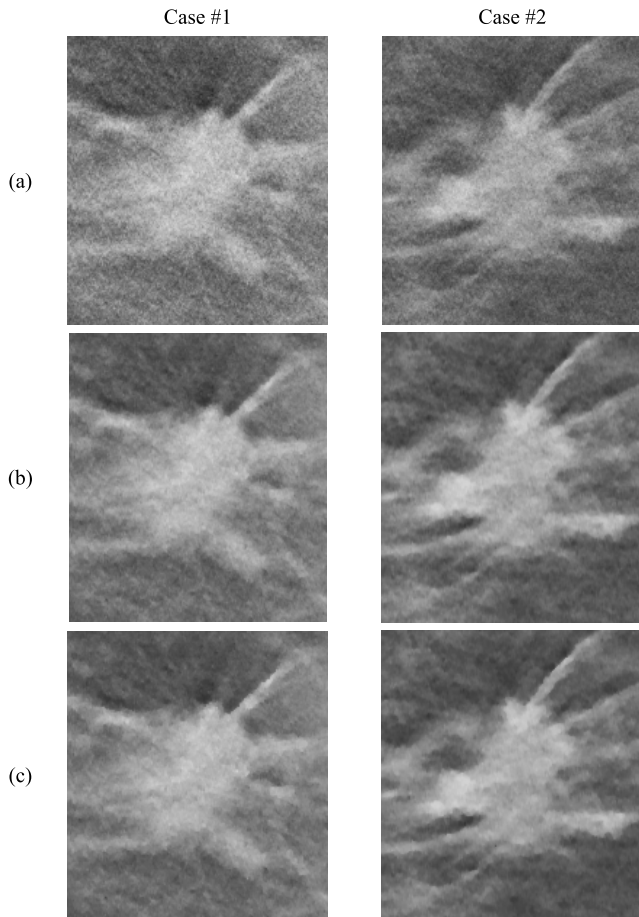

Fig. 4. Comparison of reconstruction methods and parameters using human subject DBTs with invasive ductal carcinomas. Row (a) SART, (b) SQS-DBCN, $\beta = 70$, $\delta = 0.002$/mm, (c) SQS-DBCN, $\beta = 100$, $\delta = 0.001$/mm. All image patches shown are 180×200 pixels in size. The CNR of the MCs increases from (a) to (c). However, the spiculations and the tissue textures become more patchy and artificial in (c). All images are displayed with the same window width setting.

effects compared with SART, it gives the texture a patchy appearance (Fig. 4(c)). After visually comparing the images for a range of δ and β values and considering both the MC enhancement and the appearance of the soft tissue structure, we empirically chose $\beta = 70$ and $\delta = 0.002$/mm for the SQS-DBCN algorithm. This parameter pair has a slightly larger β than the "optimal" value for MC enhancement at $\delta = 0.002$/mm, but the soft tissue texture is less patchy as shown in Fig. 4(b). Large β value also reduces spurious salt-and-pepper noise.

B. Effects of Detector Blur and Correlation Modeling

We compared the performance of SQS-DBCN with SQS-noDB and SQS-noNC for MC enhancement. Fig. 5 shows the dependence of CNR on β values at $\delta = 0.002$/mm for these three different methods, together with the CNR level of SART as a reference. When δ is fixed at other values, $\delta = 0.001$/mm or 0.003/mm, the CNR-vs-β curves of the three methods (not shown) have a similar trend as Fig. 5. Fig. 5 indicates that, compared with SQS-noDB and SQS-noNC, SQS-DBCN can achieve a much higher CNR over a wide range of β, providing more flexible choice of β to preserve the texture quality while enhancing the MCs. Compared with SART, the SQS-noDB and SQS-noNC can still provide enhancement for MCs within a small range of β values. Similar to the SQS-DBCN method, by visual evaluation of soft tissue texture we observed that using a slightly larger β than the optimal value yielded better texture quality with a tradeoff in MC enhancement. Therefore we chose to use $\beta = 40$ for SQS-noDB and $\beta = 30$ for SQS-noNC in the following discussions.

To further investigate the importance of the edge-preserving hyperbola regularization and the detector blur modeling for enhancing the MCs and preserving tissue texture in DBT reconstruction, we compared the SQS-DBCN using quadratic regularization with and without detector blur modeling. Details can be found in Section XI of the Supplementary Material. We found that, with quadratic regularization, a single β cannot provide good image quality for both MCs and tissue texture or mass margin, which is crucial for DBT reconstruction. In addition, the proposed detector blur modeling improves both the image sharpness and the CNR of MCs in comparison to without detector blur modeling. The experiments therefore
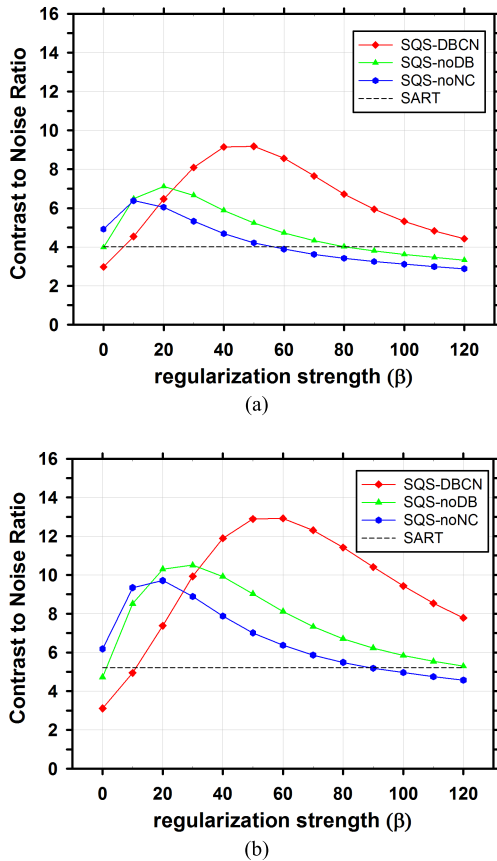
small-sized and medium sized MCs, the optimal parameter selection is about $\beta = 100$ and $\delta = 0.001$/mm. Fig. 4 shows image patches from two DBTs containing spiculated invasive ductal carcinoma from a human subject reconstructed using the SART algorithm and SQS-DBCN with two sets of parameters as examples, one of which is $\beta = 100$, $\delta = 0.001$/mm. Although this set of parameter provides superior denoising

Fig. 5. Comparison of reconstruction with different model components. CNR is plotted as a function of β at $\delta = 0.002/$mm. (a) MCs of nominal size 0.15-0.18mm, (b) MCs of nominal size 0.18-0.25mm. The SQS-DBCN method yields MCs with higher CNR compared with the SQS-noDB or the SQS-noNC reconstruction over a wide range of β values.

indicate that detector blur modeling is important for DBT reconstruction regardless of whether edge-preserving regularization is used.

C. Reconstructed MC Clusters Breast Phantom

Fig. 6 shows the reconstructed images for two MC clusters with SART, SQS-DBCN, SQS-noDB and SQS-noNC. Because the SART method does not have explicit regularization, we stopped with 3 iterations to avoid noise amplification. The mean FWHMs and the CNRs calculated for these clusters reconstructed with the different methods are also shown. Compared with SART, the MC clusters by the SQS-DBCN method are sharper on a much less noisy background. Benefiting from the denoising effect of the regularization, the SQS-noDB and the SQS-noNC methods are also able to enhance the MCs. All three methods provide higher CNRs than SART. However, the SQS-noDB method generates coarser texture in the background, while the SQS-noNC images are more blurred with "bumpy" background texture. The MCs reconstructed by the SQS-DBCN method have smaller FWHMs than those by the SART method, indicating that the MCs are sharper. On the other hand, the MCs reconstructed by the SQS-noDB and the SQS-noNC methods are more blurred, as indicated by the larger FWHMs. Among the four different methods, the

SQS-DBCN method provides the best CNR enhancement and the sharpest MCs along with smoother background texture.

To make a more quantitative comparison, we calculated the mean CNR and mean FWHM of the set of over 30 MCs in each size range. Fig. 7 shows the mean values of both FOMs and their standard deviations for the four reconstructed methods. Compared with SART, SQS-DBCN generates more conspicuous and sharper MCs (see examples in Fig. 6), as indicated by higher CNRs and smaller FWHMs. For the small MCs (0.15-0.18mm), the mean CNR increases by 90.3% from 4.02 to 7.65 when using the SQS-DBCN reconstruction. The mean CNRs increase by 136.0% and 205.5% for the medium and large MCs, respectively. The sharper and more conspicuous MCs in the SQS-DBCN images are expected to be detected more easily by radiologists or by machine vision. The mean CNRs of MCs reconstructed with the SQS-noNC and the SQS-noDB methods are also higher than those with SART, due to the enhancement of the signals with more iterations while the regularization controls the noise in the background. The mean FWHMs of these two methods, on the other hand, become almost homogenized for three different sized MCs, indicating the blurring of the reconstructed images.

Fig. 8 compares the rotationally averaged NPS of the background of the phantom DBT reconstructed with the four methods. Compared to SART, the SQS-DBCN, SQD-noDB, and SQS-noNC methods reduce the high-frequency noise but increase the lower frequency noise. The SQS-noNC method with $\beta = 30$, $\delta = 0.002/$mm causes the largest changes in the NPS, which result in the blurry and bumpy background texture. The SQS-DBCN method with the selected parameters $\beta = 70$, $\delta = 0.002/$mm changes the NPS moderately, corresponding to the less patchy texture on the images.

In addition to the heterogeneous phantom, we also used the ACR phantom and a uniform Lucite phantom to study the difference between SART and SQS-DBCN. The observations for the ACR phantom are similar to that for the heterogeneous phantom, as described in Section XII of the Supplementary Material.

D. Human Subject DBT

To evaluate the visual quality of the tissue texture, we applied SQS-DBCN to the human subject DBT images. Fig. 9 shows examples of masses reconstructed from the four different methods. The parameters used here are the same as what have been used for the phantom. Similar to the phantom images, the SQS-DBCN method is able to reduce noise compared with SART; the MCs appear to be the sharpest and have the highest contrast among the four methods. When one of the model components is ignored, although the contrasts of the MCs still appear higher than those of the SART, they are more blurry and the tissue texture becomes coarser, affecting the appearance of the mass margin.

V. DISCUSSION

In this study, we proposed a new SQS-DBCN reconstruction method for DBT applications. By accounting for the detector blur and the correlated noise model, the SQS-DBCN method
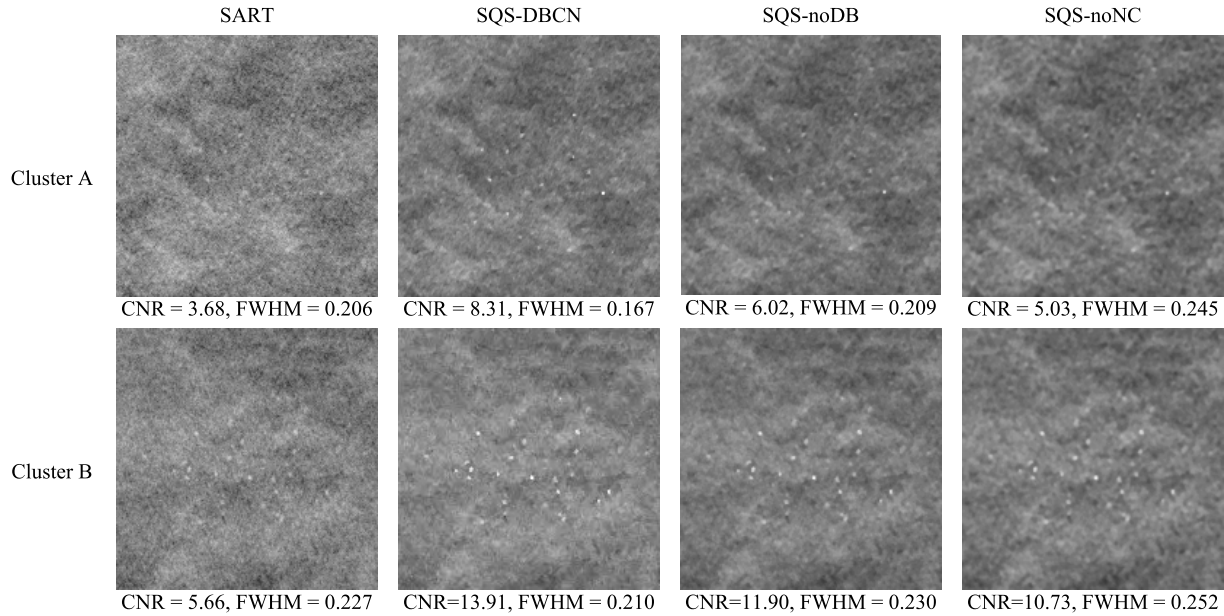
	SART	SQS-DBCN	SQS-noDB	SQS-noNC

Cluster A

| CNR = 3.68, FWHM = 0.206 | CNR = 8.31, FWHM = 0.167 | CNR = 6.02, FWHM = 0.209 | CNR = 5.03, FWHM = 0.245 |

Cluster B

| CNR = 5.66, FWHM = 0.227 | CNR=13.91, FWHM = 0.210 | CNR=11.90, FWHM = 0.230 | CNR=10.73, FWHM = 0.252 |

Fig. 6. Comparison of MC clusters reconstructed by four methods. The size of these image patches is 180×180 pixels. Cluster A: nominal size 0.15-0.18 mm, Cluster B: nominal size 0.18-0.25 mm. The SART method used 3 iterations. The CNR and FWHM (mm) are mean values of MCs from the clusters shown here. The parameters used for the SQS-DBCN method were $\beta = 70$, $\delta = 0.002$/mm. The last two columns show the reconstructed MC cluster when one of the model components was removed. The parameters used for SQS-noDB were $\beta = 40$, $\delta = 0.002$/mm, and for SQS-noNC were $\beta = 30$, $\delta = 0.002$/mm. All SQS reconstructions were run for 10 iterations. The images of the same cluster are displayed with the same window width setting.
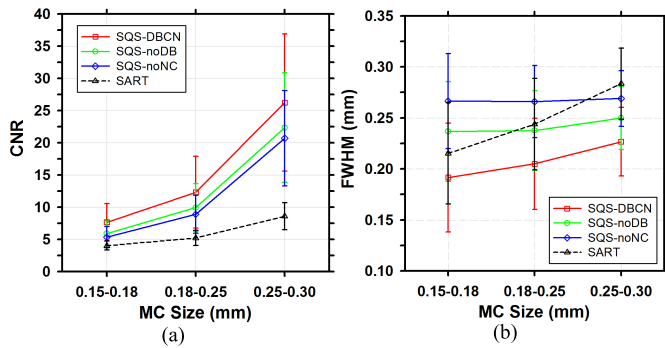

Fig. 7. Comparison of the (a) mean CNR and (b) mean FWHM averaged over MCs sampled from all clusters in the phantom. The error bars represent the standard deviations of CNR or FWHM for all MC samples of a given size.
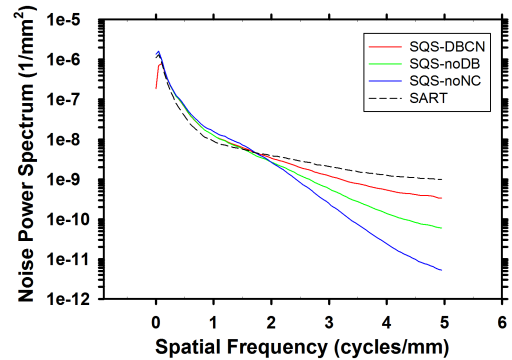
Fig. 8. Dependence of NPS on reconstruction methods: SQS-DBCN ($\beta = 70$, $\delta = 0.002$/mm), SQS-noDB ($\beta = 40$, $\delta = 0.002$/mm), SQS-noNC ($\beta = 30$, $\delta = 0.002$/mm) and SART. The NPS curves of SQS-DBCN and SQS-noDB overlaps in the low-frequency range.

is able to improve the reconstruction quality of DBT images both visually and quantitatively.

Parameter selection is a crucial step for achieving good image quality with the SQS-DBCN method. We investigated using the CNR of MCs as an FOM for guiding parameter optimization. We found that this FOM has limitations. First, CNR does not consider the spurious enhancement of noise points that may cause false MCs, which often occurs concurrently with strong enhancement of high frequency signals such as MCs. In this study, the CNR values are measured at known MC locations. If a reconstruction generates false MCs, it will not be penalized by the CNR values. Second, MCs are not the only sign of breast cancer; radiologists also need to recognize important signs such as architectural distortion or subtle spiculations from non-calcified lesions in the breast. Some reconstruction methods or parameter combinations can

generate strong artifacts on the tissue texture, as observed in CT [49]. As a result, CNR curves provide only an approximate guide for selecting parameters. As shown in Fig. 2, there is a wide range of β values where the SQS-DBCN method outperforms the SART method for enhancing the CNR of MCs. We used the parameters within this range to reconstruct human subject images and compared the visual quality of the soft tissue texture among these selections. We found that $\delta = 0.002$/mm, $\beta = 70$ is a reasonable choice for the SQS-DBCN method that does not cause strong artifacts and only trades off a fraction of the MC enhancement.

One challenge in the parameter selection is that different cases may require different parameter combinations for the best image quality due to the variations in the noise level of images. For the phantom DBT, we can use the CNR of MCs to guide the parameter selection. However,
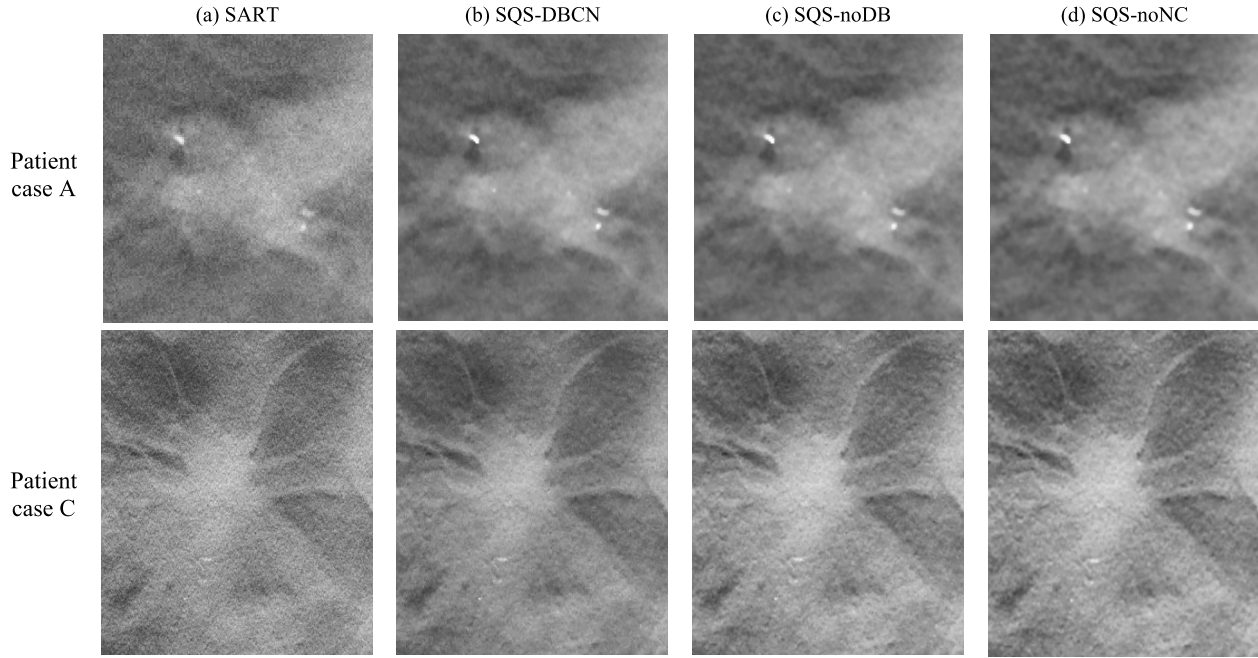
Fig. 9. Comparison of four methods using human subject DBT images with invasive ductal carcinomas. The sizes of the image patches are 150 × 160 pixels (top row) and 300 × 360 pixels (bottom row). The SART method used 3 iterations. The parameters were $\beta = 70$, $\delta = 0.002/mm$ for the SQS-DBCN method, $\beta = 40$, $\delta = 0.002/mm$ for the SQS-noDB method, and $\beta = 30$, $\delta = 0.002/mm$ for the SQS-noNC method. All SQS methods were run for 10 iterations. All images are displayed with the same window width setting.

the selected parameters may not work well for some patient cases. It is difficult to define an FOM for a patient case to help parameter selection because the target lesion of a given patient case is usually unknown. For this reason, we implemented the adaptive parameter adjustment as shown in (13) and (14). Only β is adjusted in the procedure while the value of δ is fixed. We will continue to investigate the strategy for adaptively adjusting the parameters to further improve the image quality for patient cases when using the SQS-DBCN method.

One may tend to use quadratic regularization to avoid δ in the potential function and to reduce the number of hyper-parameters by one. However, our experiments (Section XI of the Supplementary Material) indicate that the hyperbola regularization is superior to quadratic regularization for DBT reconstruction because of the dual roles played by the hyperbola potential function $\eta(t) = \delta^2\left(\sqrt{1 + (t/\delta)^2} - 1\right)$. For reconstructing soft tissue, the difference between neighboring pixels is small such that $\delta = 0.002/mm$ is large enough for the potential function to work in the 'quadratic' part of the curve. It therefore behaves like quadratic regularization that produces relatively smooth and natural soft tissue texture at large β. For MCs with high gradient between neighboring pixels, the potential function behaves like linear regularization such that MCs are preserved even when relatively strong regularization with large β is used to reduce noise. The property of the hyperbola function thus matches well with the requirements for DBT reconstruction.

The comparison of SQS-DBCN, SQS-noDB and SQS-noNC demonstrates that the effectiveness of the SQS-DBCN method relies on the completeness of all three model components: detector blur, noise correlation and regularization. Although

intuitively, the MC enhancement might result from the deblur-ring effect of modeling detector blur, our results with the SQS-noNC method demonstrate that modeling noise correlation is equally important. Our comparison of SQS-DBCN with the PWLS reconstruction algorithm used in CT (see Section IX in Supplementary Material) further indicates that statistical iterative reconstruction methods developed for CT are not sufficient for DBT because they ignore detector blur and noise correlation. Similar to the SQS-DBCN method, parameters of SQS-noDB and SQS-noNC methods were chosen based on both the CNR performance and the soft tissue texture. We found that over the range of β values where the CNR is relatively high ($\beta = 10$ to 40 for SQS-noDB and $\beta = 10$ to 30 for SQS-noNC), it is more difficult to find a proper β with satisfactory tissue texture. As shown in Fig. 7(a), with the chosen β values for these two methods, the mean CNRs for MCs of all three sizes are lower than those of the SQS-DBCN method. Fig. 7(b) shows that with the SQS-noDB or the SQS-noNC methods, the mean FWHMs become similar for MCs of all three sizes, which is undesirable. The image patches in Fig. 6 also demonstrate that the background texture obtained with the SQS-noDB or the SQS-noNC methods looks blurry and coarse and the MCs are less sharp compared to those with the SQS-DBCN method. The reconstructed images of human subject DBT in Fig. 9 support the same conclu-sion. Further comparison of SQS-DBCN and SQS-noDB with quadratic regularization also leads to similar observations as discussed in Section XI of the Supplementary Material. These results indicate that both the detector blur and the correlated noise modeling in the SQS-DBCN method are important components in the reconstruction and that its superior CNR performance is not simply a result of the regularization.

Another interesting observation is that the SQS-noDB method generally performs better than the SQS-noNC method. Fig. 6 shows that the SQS-noNC images looks more blurry compared with the SQS-noDB images. Fig. 7 shows that the SQS-noNC method gives lower CNR values and larger FWHM values for all three different-sized MCs. In fact, the SQS-noDB method is equivalent to the SQS-DBCN method if the true point spread function of the detector blur is a Kronecker impulse. For the SQS-noDB method, although the detector blur is ignored, the noise model still matches the forward model in the data-fitting term of (6). On the other hand, the SQS-noNC method incorporates the detector blur in the forward model and ignores the corresponding noise correlation. The results reveal that such a mismatch in the modeling degrades image quality. The comparison between SQS-noDB and SQS-DBCN indicates the importance of the noise correlation model.

There are a number of limitations for this preliminary study of an MBIR method for DBT. The SQS-DBCN method depends on several approximations. We approximate the detector blur as linear shift-invariant for a given projection and as independent of the x-ray incident angle to the detector. The reconstructed object approximately consists of a relatively uniform background, where the fibrous tissue and MCs are treated as high-frequency structures embedded in the background. We also treat the quantum noise to be relatively constant over the field of view for a given projection angle. The model for the SQS-DBCN method only includes the detector blur and the corresponding noise correlation. Other factors such as x-ray focal spot blur, beam hardening and scatter are not considered in our current model. However, even with such a simplified model and approximations, the SQS-DBCN method enhances MCs and suppresses noise compared to SART reconstruction, while preserving tissue texture and mass spiculations for low-dose DBT scans. The SQS-DBCN implementation not only provides a practical DBT reconstruction method, but also indicates the potential value of model-based image reconstruction for DBT. We are currently working on a more detailed model of the system and relaxing the approximations used to simplify the reconstruction algorithm.

VI. Conclusion

We proposed a DBT reconstruction method that incorporates detector blur and a correlated noise model as the first step towards developing an MBIR method for DBT. We have shown quantitatively and qualitatively that the new SQS-DBCN method can better enhance MCs compared with SART while preserving the image quality of mass spiculations and tissue texture. We have also demonstrated the effectiveness of the SQS-DBCN method as a result of incorporating the detector blur, the noise correlation and the regularization at the same time, indicating that a more complete model-based reconstruction may further improve the DBT image quality.

References

[1] L. T. Niklason *et al.*, "Digital tomosynthesis in breast imaging," *Radiology*, vol. 205, no. 2, pp. 399–406, 1997.

[2] T. Wu *et al.*, "Tomographic mammography using a limited number of low-dose cone-beam projection images," *Med. Phys.*, vol. 30, no. 3, pp. 365–380, Mar. 2003.

[3] D. B. Kopans, "Digital tomosynthesis and other applications," in *RSNA Program Book*. Oak Brook, IL, USA: RSNA, 2005, p. 130.

[4] G. Lauritsch and W. H. Haerer, "Theoretical framework for filtered back projection in tomosynthesis," *Proc. SPIE*, vol. 3338, pp. 1127–1137, Jun. 1998.

[5] B. E. H. Claus, J. W. Eberhard, A. Schmitz, P. Carson, M. Goodsitt, and H.-P. Chan, "Generalized filtered back-projection reconstruction in breast tomosynthesis," in *Digital Mammography* (Lecture Notes in Computer Science), vol. 4046. Berlin, Germany: Springer-Verlag, 2006, pp. 167–174.

[6] T. Mertelmeier, J. Orman, W. Haerer, and M. K. Dudam, "Optimizing filtered backprojection reconstruction for a breast tomosynthesis proto-type device," *Proc. SPIE*, vol. 6142, p. 61420F, Mar. 2006.

[7] Y.-H. Hu, B. Zhao, and W. Zhao, "Image artifacts in digital breast tomosynthesis: Investigation of the effects of system geometry and reconstruction parameters using a linear system approach," *Med. Phys.*, vol. 35, no. 12, pp. 5242–5252, Dec. 2008.

[8] G. J. Gang, D. J. Tward, J. Lee, and J. H. Siewerdsen, "Anatomical background and generalized detectability in tomosynthesis and cone-beam CT," *Med. Phys.*, vol. 37, no. 5, pp. 1948–1965, May 2010.

[9] I. Sechopoulos, "A review of breast tomosynthesis. Part II. Image reconstruction, processing and analysis, and advanced applications," *Med. Phys.*, vol. 40, no. 1, p. 014302, Jan. 2013.

[10] Y. Zhang *et al.*, "A comparative study of limited-angle cone-beam reconstruction methods for breast tomosynthesis," *Med. Phys.*, vol. 33, no. 10, pp. 3781–3795, Oct. 2006.

[11] E. Y. Sidky, X. Pan, I. S. Reiser, R. M. Nishikawa, R. H. Moore, and D. B. Kopans, "Enhanced imaging of microcalcifications in digital breast tomosynthesis through improved image-reconstruction algorithms," *Med. Phys.*, vol. 36, no. 11, pp. 4920–4932, Nov. 2009.

[12] M. Das, H. C. Gifford, J. M. O'Connor, and S. J. Glick, "Penalized maximum likelihood reconstruction for improved microcalcification detection in breast tomosynthesis," *IEEE Trans. Med. Imag.*, vol. 30, no. 4, pp. 904–914, Apr. 2011.

[13] J. G. Bian, K. Yang, J. M. Boone, X. Han, E. Y. Sidky, and X. Pan, "Investigation of iterative image reconstruction in low-dose breast CT," *Phys. Med. Biol.*, vol. 59, no. 11, pp. 2659–2685, 2014.

[14] E. Haneda *et al.*, "Toward a dose reduction strategy using model-based reconstruction with limited-angle tomosynthesis," *Proc. SPIE*, vol. 9033, p. 90330V, Mar. 2014.

[15] E. Samei, J. Thompson, S. Richard, and J. Bowsher, "A case for wide-angle breast tomosynthesis," *Acad. Radiol.*, vol. 22, no. 7, pp. 860–869, Jul. 2015.

[16] K. Lange and J. A. Fessler, "Globally convergent algorithms for maximum *a posteriori* transmission tomography," *IEEE Trans. Image Process.*, vol. 4, no. 10, pp. 1430–1438, Oct. 1995.

[17] I. A. Elbakri and J. A. Fessler, "Statistical image reconstruction for polyenergetic X-ray computed tomography," *IEEE Trans. Med. Imag.*, vol. 21, no. 2, pp. 89–99, Feb. 2002.

[18] J.-B. Thibault, K. D. Sauer, C. A. Bouman, and J. Hsieh, "A three-dimensional statistical approach to improved image quality for multislice helical CT," *Med. Phys.*, vol. 34, no. 11, pp. 4526–4544, 2007.

[19] B. De Man and J. A. Fessler, "Statistical iterative reconstruction for X-ray computed tomography," in *Biomedical Mathematics: Promising Directions in Imaging, Therapy Planning, and Inverse Problems*, Y. Censor, M. Jiang and G. Wang, Eds. Madison, WI, USA: Medical Physics Publishing, 2010, pp. 113–140.

[20] J. Nuyts, B. De Man, J. A. Fessler, W. Zbijewski, and F. J. Beekman, "Modelling the physics in the iterative reconstruction for transmission computed tomography," *Phys. Med. Biol.*, vol. 58, no. 12, pp. R63–R96, 2013.

[21] S. Tilley, J. H. Siewerdsen, and J. W. Stayman, "Iterative CT reconstruction using models of source and detector blur and correlated noise," in *Proc. Int. Conf. Image Form X-Ray Comput. Tomogr.*, 2014, pp. 363–367.

[22] S. Tilley, J. H. Siewerdsen, and J. W. Stayman, "Model-based iterative reconstruction for flat-panel cone-beam CT with focal spot blur, detector blur, and correlated noise," *Phys. Med. Biol.*, vol. 61, no. 1, pp. 296–319, 2016.

[23] S. Tilley, J. H. Siewerdsen, W. Zbijewski, and J. W. Stayman, "Nonlinear statistical reconstruction for flat-panel cone-beam CT with blur and correlated noise models," *Proc. SPIE*, vol. 9783, p. 97830R, Mar. 2016.

[24] K. Kim *et al.*, "Fully iterative scatter corrected digital breast tomosynthesis using GPU-based fast Monte Carlo simulation and composition ratio update," *Med. Phys.*, vol. 42, no. 9, pp. 5342–5355, Sep. 2015.

[25] S. Xu, J. Lu, O. Zhou, and Y. Chen, "Statistical iterative reconstruction to improve image quality for digital breast tomosynthesis," *Med. Phys.*, vol. 42, no. 9, pp. 5377–5390, Sep. 2015.

[26] B. De Man and S. Basu, "Distance-driven projection and backprojection in three dimensions," *Phys. Med. Biol.*, vol. 49, no. 11, pp. 2463–2475, Jun. 2004.

[27] Y. Long, J. A. Fessler, and J. M. Balter, "3D forward and back-projection for X-ray CT using separable footprints," *IEEE Trans. Med. Imag.*, vol. 29, no. 11, pp. 1839–1850, Nov. 2010.

[28] J. Zheng, J. A. Fessler, and H.-P. Chan, "Segmented separable footprint projector for digital breast tomosynthesis and its application for subpixel reconstruction," *Med. Phys.*, vol. 44, no. 3, pp. 986–1001, Mar. 2017.

[29] J. Zheng, J. A. Fessler, and H.-P. Chan, "Digital breast tomosynthesis reconstruction with detector blur and correlated noise," in *Proc. 4th Int. Conf. Image Formation X-Ray Comput. Tomography CT-Meet.*, 2016, pp. 21–24.

[30] M. Persson, D. Bone, and H. Elmqvist, "Total variation norm for three-dimensional iterative reconstruction in limited view angle tomography," *Phys. Med. Biol.*, vol. 46, no. 3, pp. 853–866, 2001.

[31] Y. Lu, H.-P. Chan, J. Wei, and L. M. Hadjiiski, "Selective-diffusion regularization for enhancement of microcalcifications in digital breast tomosynthesis reconstruction," *Med. Phys.*, vol. 37, no. 11, pp. 6003–6014, Nov. 2010.

[32] Y. Lu, H.-P. Chan, J. Wei, L. M. Hadjiiski, and R. K. Samala, "Multiscale bilateral filtering for improving image quality in digital breast tomosynthesis," *Med. Phys.*, vol. 42, no. 1, pp. 182–195, Jan. 2015.

[33] J. Zheng, J. A. Fessler, and H.-P. Chan, "Digital breast tomosynthesis reconstruction using spatially weighted non-convex regularization," *Proc. SPIE*, vol. 9783, p. 978369, Mar. 2016.

[34] H. Erdogan and J. A. Fessler, "Ordered subsets algorithms for transmission tomography," *Phys. Med. Biol.*, vol. 44, no. 11, pp. 2835–2851, 1999.

[35] D. Kim, D. Pal, J. B. Thibault, and J. A. Fessler, "Accelerating ordered subsets image reconstruction for X-ray CT using spatially nonuniform optimization transfer," *IEEE Trans. Med. Imag.*, vol. 32, no. 11, pp. 1965–1978, Nov. 2013.

[36] K. Sauer and C. Bouman, "A local update strategy for iterative reconstruction from projections," *IEEE Trans. Signal Process.*, vol. 41, no. 2, pp. 534–548, Feb. 1993.

[37] R. García-Mollá, R. Linares, and R. Ayala, "Study of DQE dependence with beam quality on GE essential mammography flat panel," *J. Appl. Clin. Med. Phys.*, vol. 12, no. 1, p. 3176, 2010.

[38] E. Samei, M. J. Flynn, and D. A. Reimann, "A method for measuring the presampled MTF of digital radiographic systems using an edge test device," *Med. Phys.*, vol. 25, no. 1, pp. 102–113, 1998.

[39] Y. T. Wu *et al.*, "Dynamic multiple thresholding breast boundary detection algorithm for mammograms," *Med. Phys.*, vol. 37, no. 1, pp. 391–401, Jan. 2010.

[40] H. R. Shi and J. A. Fessler, "Quadratic regularization design for 2-D CT," *IEEE Trans. Med. Imag.*, vol. 28, no. 5, pp. 645–656, May 2009.

[41] H. M. Hudson and R. S. Larkin, "Accelerated image reconstruction using ordered subsets of projection data," *IEEE Trans. Med. Imag.*, vol. 13, no. 4, pp. 601–609, Dec. 1994.

[42] M. S. Andersen and P. C. Hansen, "Generalized row-action methods for tomographic imaging," *Numer. Algorithms*, vol. 67, no. 1, pp. 121–144, Sep. 2014.

[43] D. Van de Sompel, S. M. Brady, and J. Boone, "Task-based performance analysis of FBP, SART and ML for digital breast tomosynthesis using signal CNR and channelised hotelling observers," *Med. Image Anal.*, vol. 15, no. 1, pp. 53–70, Feb. 2011.

[44] R. I. Siddon, "Fast calculation of the exact radiological path for a three-dimensional CT array," *Med. Phys.*, vol. 12, pp. 252–255, Mar. 1985.

[45] Y. Zhang *et al.*, "Artifact reduction methods for truncated projections in iterative breast tomosynthesis reconstruction," *J. Comput. Assist. Tomography*, vol. 33, no. 3, pp. 426–435, 2009.

[46] Y. Lu, H.-P. Chan, J. Wei, and L. M. Hadjiiski, "A diffusion-based truncated projection artifact reduction method for iterative digital breast tomosynthesis reconstruction," *Phys. Med. Biol.*, vol. 58, no. 3, pp. 569–587, 2013.

[47] L. Tabar and P. B. Dean, *Teaching Atlas of Mammography*, New York, NY, USA: Thieme, 1985.

[48] H. P. Chan *et al.*, "Digital breast tomosynthesis: Observer performance of clustered microcalcification detection on breast phantom images acquired with an experimental system using variable scan angles, angular increments, and number of projection views," *Radiology*, vol. 273, no. 3, pp. 675–685, 2014.

[49] F. E. Boas and D. Fleischmann, "CT artifacts: Causes and reduction techniques," *Imag. Med.*, vol. 4, no. 2, pp. 229–240, 2012.

Detector Blur and Correlated Noise Modeling for Digital Breast Tomosynthesis Reconstruction
Supplementary Material

Jiabei Zheng*, *Member, IEEE*, Jeffrey A. Fessler*, *Fellow, IEEE*, Heang-Ping Chan[†]

This supplement provides additional information and supporting data for the paper 'Detector Blur and Correlated Noise Modeling for Digital Breast Tomosynthesis Reconstruction' by Jiabei Zheng, Jeffrey A. Fessler and Heang-Ping Chan. The number of sections, equations and figures follow sequentially from those in the paper.

VII. Derivation of noise covariance $\mathbf{K}_i$

The derivation of the noise covariance $\mathbf{K}_i$ of the ith projection view in Equation (5) is similar to the Appendix of Tilley et al. [22]; the difference is that our application is for DBT geometry in which the imaged volume is very close to the detector. As a result, we neglect the focal spot blur so the blurring operation $\mathbf{B}_i$ in our study only includes the detector blur. For the directly measured projection $\mathbf{Y}_i$ before the log transform, we treat it as having a Gaussian distribution:

$$\mathbf{Y}_i \sim N\left(\overline{\mathbf{Y}}_i, \mathbf{K}_i^Y\right), \tag{32}$$

where

$$\overline{\mathbf{Y}}_i = I_0 \mathbf{B}_i \exp\left(-\mathbf{A}_i \mathbf{f}\right), \tag{33}$$

$$\mathbf{K}_i^Y = \mathbf{B}_i \mathbf{K}_i^Q \mathbf{B}_i' + \mathbf{K}_i^R, \tag{34}$$

where the capital letters Q and R in the superscripts denote that these values are for the projections before the log transform.

According to Equation (1) - (3) in Section II.A of the paper, we have:

$$\overline{\mathbf{Y}}_i \approx I_0 \exp\left(-\mathbf{B}_i \mathbf{A}_i \mathbf{f}\right). \tag{35}$$

The expectation of the log-transformed projection $\mathbf{y}_i$ is approximately:

$$\overline{\mathbf{y}}_i = \log\left(\frac{I_0}{\overline{\mathbf{Y}}_i}\right) \approx \mathbf{B}_i \mathbf{A}_i \mathbf{f}. \tag{36}$$

Similar to Tilley et al. [22], we consider the fluctuation of the random noise to be small compared with the mean value:

$$\frac{\mathbf{Y}_i - \overline{\mathbf{Y}}_i}{\overline{\mathbf{Y}}_i} \ll 1. \tag{37}$$

Then we have:

$$\mathbf{y}_i = \log\left(\frac{I_0}{\mathbf{Y}_i}\right)$$

$$= \log\left(\frac{I_0}{\overline{\mathbf{Y}}_i}\right) - \log\left(1 + \frac{\mathbf{Y}_i - \overline{\mathbf{Y}}_i}{\overline{\mathbf{Y}}_i}\right) \tag{38}$$

$$\approx \overline{\mathbf{y}}_i - \frac{\mathbf{Y}_i - \overline{\mathbf{Y}}_i}{\overline{\mathbf{Y}}_i}.$$

As a result, $\mathbf{y}_i$ also follows approximately a Gaussian distribution:

$$\mathbf{y}_i \sim N(\overline{\mathbf{y}}_i, \mathbf{K}_i), \tag{39}$$

where

$$\mathbf{K}_i = \text{diag}\left(\frac{1}{\overline{\mathbf{Y}}_i}\right) \mathbf{B}_i \mathbf{K}_i^Q \mathbf{B}_i' \text{diag}\left(\frac{1}{\overline{\mathbf{Y}}_i}\right) + \text{diag}\left(\frac{1}{\overline{\mathbf{Y}}_i}\right) \mathbf{K}_i^R \text{diag}\left(\frac{1}{\overline{\mathbf{Y}}_i}\right). \tag{40}$$

In our application, the blurring kernel $\mathbf{h}_i$ is symmetric along the horizontal and vertical directions. So $\mathbf{B}_i$ is a symmetric matrix. As we discussed in Section II.A, we assume the low-frequency background to be approximately uniform over the support of the blurring kernel while a small structure such as MC contributes only a small amount of projection values. As a result, $\overline{\mathbf{Y}}_i$ is approximately uniform over the support of the blurring kernel. Thus we make the following approximation:

$$\text{diag}\left(\frac{1}{\overline{\mathbf{Y}}_i}\right) \mathbf{B}_i \approx \mathbf{B}_i \text{diag}\left(\frac{1}{\overline{\mathbf{Y}}_i}\right). \tag{41}$$

The covariance matrix $\mathbf{K}_i$ then simplifies as:

$$\mathbf{K}_i \approx \mathbf{B}_i \text{diag}\left(\frac{1}{\overline{\mathbf{Y}}_i}\right) \mathbf{K}_i^Q \text{diag}\left(\frac{1}{\overline{\mathbf{Y}}_i}\right) \mathbf{B}_i' + \text{diag}\left(\frac{1}{\overline{\mathbf{Y}}_i}\right) \mathbf{K}_i^R \text{diag}\left(\frac{1}{\overline{\mathbf{Y}}_i}\right)$$

$$= \mathbf{B}_i \mathbf{K}_i^q \mathbf{B}_i' + \mathbf{K}_i^r, \tag{42}$$

where

$$\mathbf{K}_i^q = \text{diag}\left(\frac{1}{\overline{\mathbf{Y}}_i}\right) \mathbf{K}_i^Q \text{diag}\left(\frac{1}{\overline{\mathbf{Y}}_i}\right), \tag{43}$$

$$\mathbf{K}_i^r = \text{diag}\left(\frac{1}{\overline{\mathbf{Y}}_i}\right) \mathbf{K}_i^R \text{diag}\left(\frac{1}{\overline{\mathbf{Y}}_i}\right). \tag{44}$$

Equations (43) and (44) also indicate that when we assume $\mathbf{K}_i^q = \sigma_i^{q^2}\mathbf{I}$ and $\mathbf{K}_i^r = \sigma_i^{r^2}\mathbf{I}$, it is equivalent to assuming $\text{diag}\left(\frac{1}{\overline{\mathbf{Y}}_i}\right) \mathbf{K}_i^Q \text{diag}\left(\frac{1}{\overline{\mathbf{Y}}_i}\right)$ and $\text{diag}\left(\frac{1}{\overline{\mathbf{Y}}_i}\right) \mathbf{K}_i^R \text{diag}\left(\frac{1}{\overline{\mathbf{Y}}_i}\right)$ to be constant along the diagonal for the ith projection angle.

VIII. Justification of the Approximation of Constant Quantum Noise

For an efficient implementation of $\mathbf{S}_i$, the inverse square root of the covariance matrix, we treat the quantum noise standard deviation σ_i^q as approximately a constant for each given projection angle. To illustrate the effect of this approximation, we simulated a breast phantom with CatSim [50, 51] (GE Global Research, Niskayuna, NY) to estimate the range of σ_i^q. We did not include readout noise so that the estimation below simulates the situation where the readout noise component is perfectly separated from the quantum noise component (Section II.B and Equation (12)). The geometry of the simulated DBT system matches the geometry of the experimental system shown in Fig. 1. The phantom consists of a half cylinder of fatty tissue embedded with a small cylinder of glandular tissue (Fig. 10). The radius of the half

cylinder is 6 cm and the radius of the small cylinder is 2 cm. The thickness of both blocks of material is 5 cm. The phantom simulates a compressed breast of an average thickness with glandular and fatty tissue regions such that the dynamic range of the transmitted x-ray intensities incident on the detector approximates an extreme situation. In a real breast, the glandular tissue and fatty tissue are heterogeneously mixed so that the range will be within this extreme. Fig. 11 shows simulated projections at scan angle $\theta = -12°, 0°, 12°$ of the phantom.
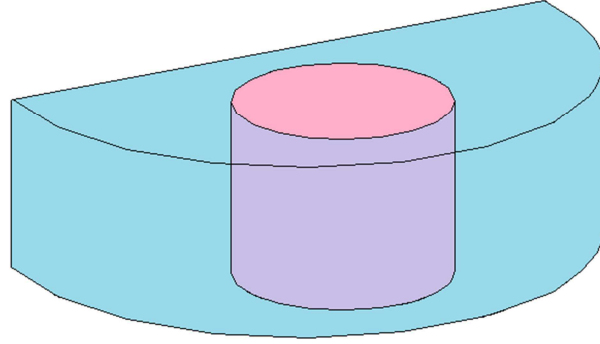
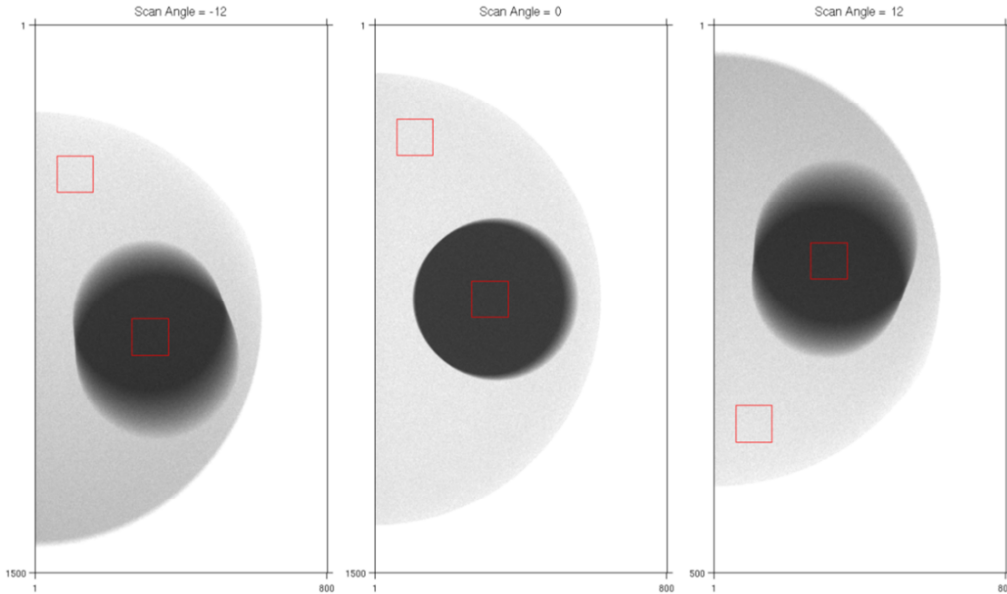Fig. 10. The simulated breast phantom with 100% glandular tissue (pink) surrounded by 100% fatty tissue (blue).

Fig. 11. Simulated projections at scan angle $\theta = -12°, 0°, 12°$. The red boxes mark the locations for estimating the range of σ_i^q.

Table 1: The range of σ_i^q

Projection angle	σ_i^q behind the fatty tissue	σ_i^q behind the glandular tissue	σ_i^q(glandular)/σ_i^q(fatty)
-12	0.0666	0.1369	2.06
0	0.0651	0.1284	1.97
12	0.0659	0.1378	2.09

The range of σ_i^q is estimated from the patches marked with red boxes in Fig. 11. Table 1 shows the results. According to Table 1, the ratio between the maximum σ_i^q and minimum σ_i^q for a given projection angle could be as large as 2.09. Therefore, when we use the σ_i^q value averaged over the entire projection view to represent the noise in our SQS-DBCN reconstruction for a human breast image, the error in treating the noise variance as a constant may range from overestimating σ_i^q by 100% to underestimating σ_i^q by 50% in local regions of the projection view.

We therefore studied the effect of noise estimation error by an amount varying between these two worst-case scenarios. We multiplied all estimated σ_i^q by an 'estimation factor', denoted as τ, to simulate the cases where we overestimate or underestimate the values of σ_i^q. We performed a series of reconstructions for our breast phantom with clusters of MCs (described in Section III.B), by varying the range of τ from 0.5 to 2, while keeping the other parameters the same ($\delta = 0.002$, $\beta = 70$). The CNR and FWHM of MCs are shown in Fig. 12. Examples of reconstructed image patches are shown in Fig. 13.
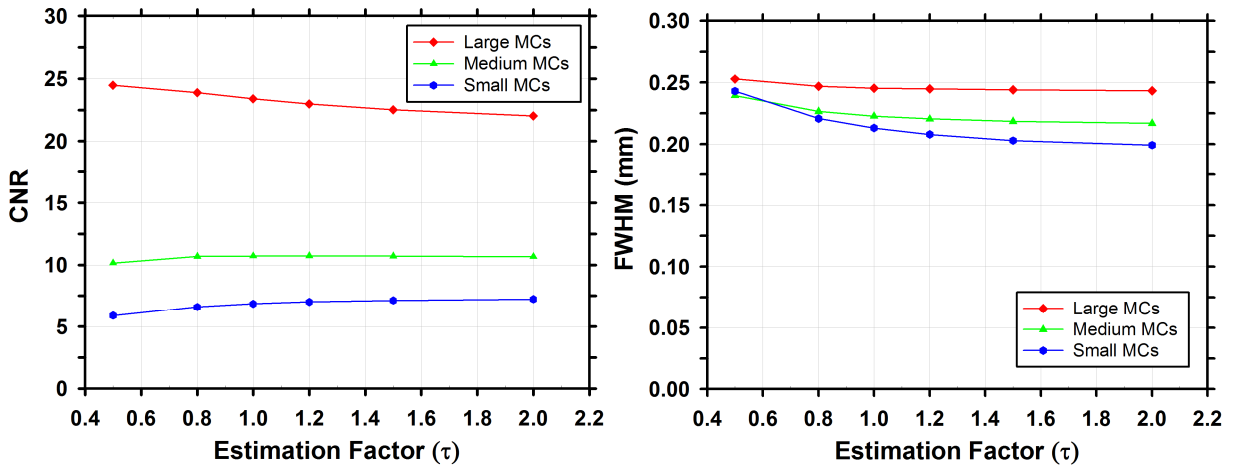

Fig. 12. CNR and FWHM curves as the estimated noise varies by a factor of τ.

Fig. 12 shows that the reconstructed CNRs of MCs are not strongly affected by small deviations from the estimation of σ_i^q. For the small MCs of nominal size 0.15-0.18 mm, the maximum change in CNR is 22% and the maximum change in FWHM is 25%. This is relatively small considering that the ratio between the maximum τ and the minimum τ is 4 in this experiment. For MCs of other sizes, the change in CNR and FWHM is even smaller. Fig. 13 shows examples of reconstructed MC patches of three different sizes. It can be observed that the quality does not change drastically even in the worst-case scenarios. As a result, using a constant σ_i^q for each projection angle is a reasonable approximation.

Despite these results, treating quantum noise variance as a constant is a limitation of our current implementation of the MBIR. The fact that the image quality obtained from our SQS-DBCN method was improved even with the simplifying approximations shows the potential of MBIR methods for DBT, but further studies are needed to continue the development and relax the assumptions.

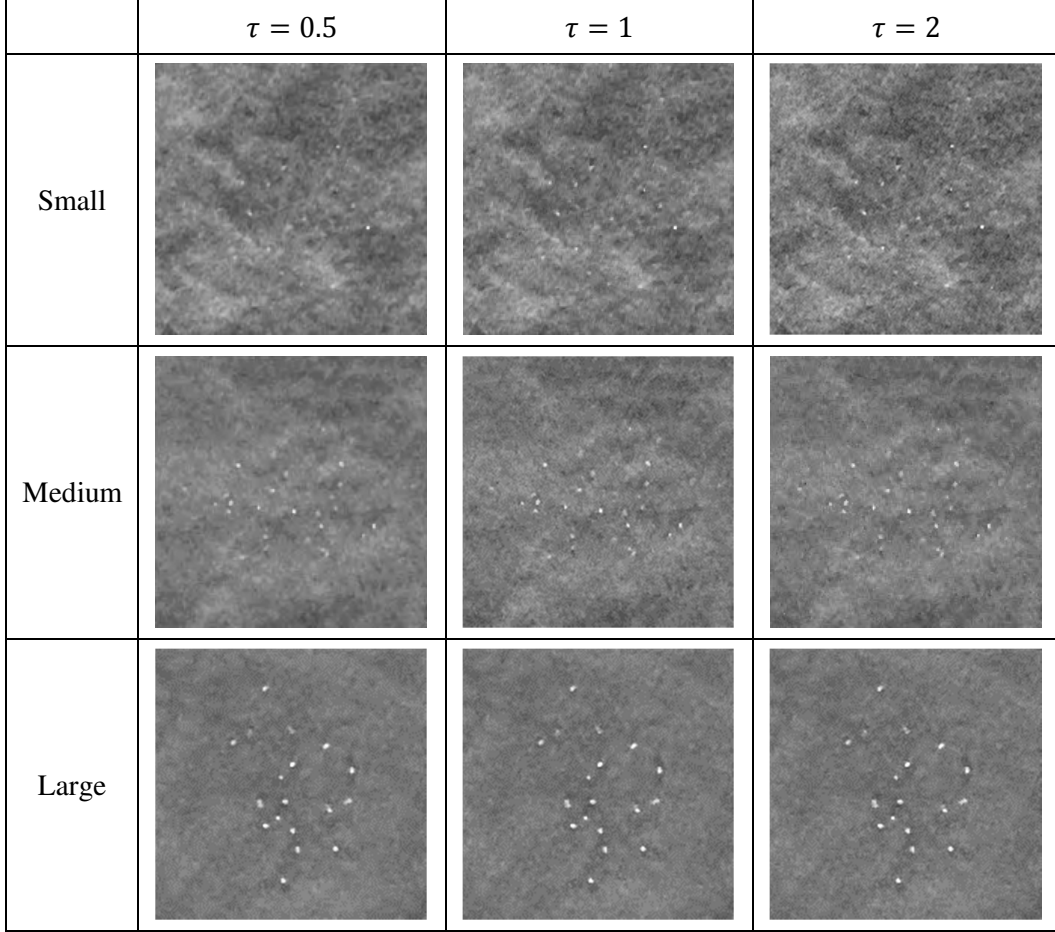|	$\tau = 0.5$	$\tau = 1$	$\tau = 2$
Small			
Medium			
Large			

Fig. 13. Reconstructed MC patches with a range of estimation factors. The images of the same cluster are displayed with the same window width setting.

IX. DBT Reconstruction with the Penalized Weighted Least-Squares Cost Function

In addition to the SQS-DBCN, SQS-noDB and SQS-noNC methods, we studied a fourth DBT reconstruction method using the penalized weighted least-squares (PWLS) cost function [18, 36]. Such a cost function is widely used in statistical iterative reconstruction for clinical CT systems where the detector pixel crosstalk can be ignored. For this implementation, we used the usual diagonal weighting matrix based on the estimated statistical variance at each detector pixel. Specifically, the PWLS cost function is:

$$\Psi_{\text{PWLS}}(\mathbf{f}) = \frac{1}{2} \sum_{i=1}^{N_{\text{p}}} \|\mathbf{y}_i - \mathbf{A}_i \mathbf{f}\|^2_{\mathbf{D}_i} + R(\mathbf{f}), \tag{45}$$

where $\mathbf{D}_i$ is a diagonal matrix. Let j denote the index of pixels for the ith projection angle, the jth element of the diagonal matrix $\mathbf{D}_i$ is:

$$\mathbf{D}_i[j] = \frac{1}{\sigma_{\mathbf{y}_i[j]}^2}, \tag{46}$$

where

$$\sigma_{\mathbf{y}_i[j]} = \frac{\sigma_{\mathbf{Y}_i[j]}}{\mathbf{Y}_i[j]} = \sqrt{\frac{1}{\mathbf{Y}_i[j]}}. \tag{47}$$

Since we are no longer using constant σ_i^{q} and σ_i^{r} in this implementation, the formula for the adaptive-regularization scaling factor α is different from Equation (14):

$$\alpha_{\mathrm{PWLS}} = \frac{1}{\sum_{i=1}^{N_{\mathrm{p}}} \sum_j \omega_{\mathbf{y}_i}[j] \sigma_{\mathbf{y}_i[j]}^2 / \sum_{i=1}^{N_{\mathrm{p}}} \sum_j \omega_{\mathbf{y}_i}[j]}, \tag{48}$$

where $\omega_{\mathbf{y}_i}[j] = 1$ if j is within the detected breast boundary [39] for the ith PV and $\omega_{\mathbf{y}_i}[j] = 0$ otherwise.

We still use the SQS algorithm to minimize the cost function $\Psi_{\mathrm{PWLS}}(\mathbf{f})$. We refer to this reconstruction algorithm as the SQS-PWLS method. The SQS-PWLS method is basically the SQS-noDB method (Equation (30)) with detector pixel location-dependent noise variance.
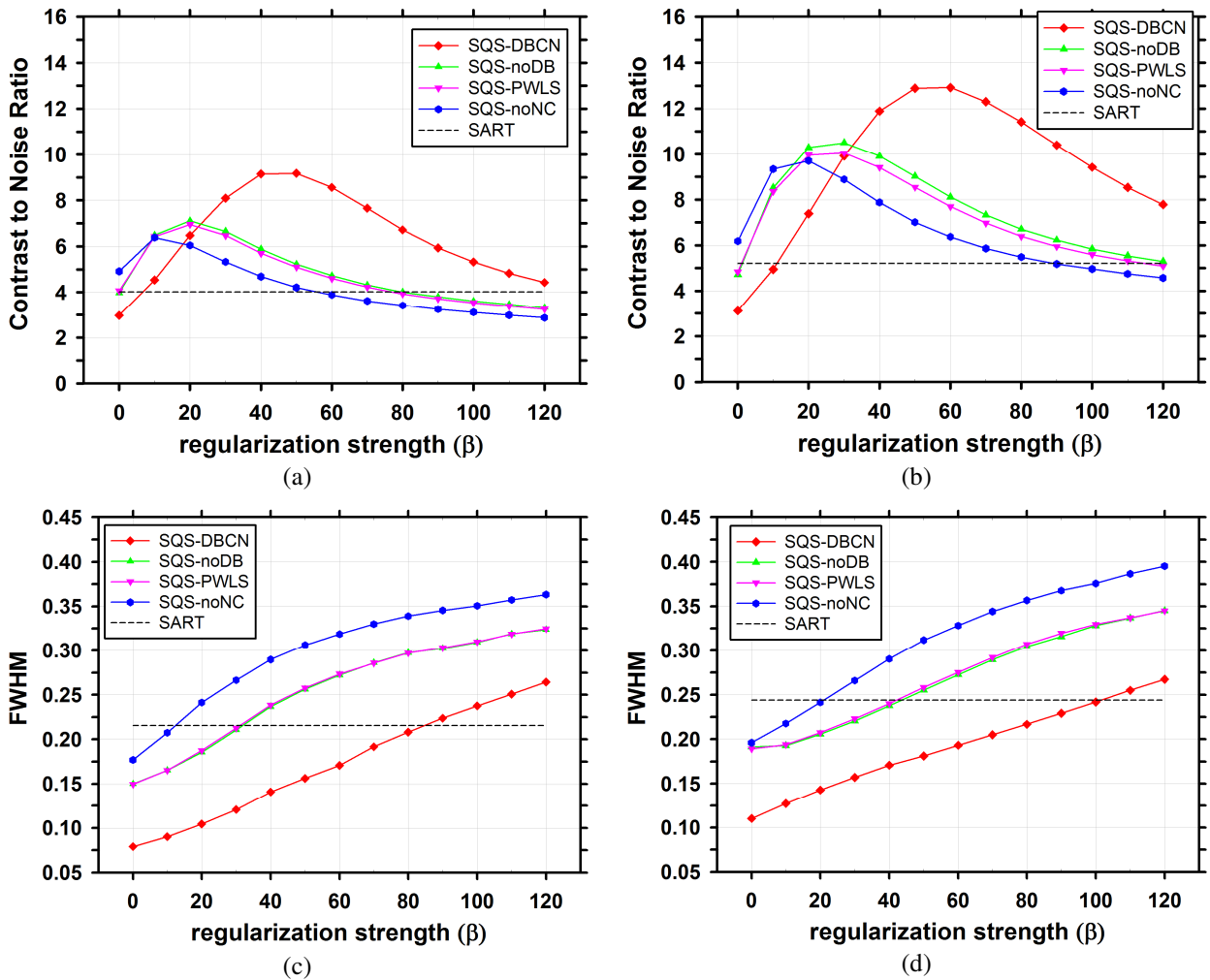

Fig. 14. Dependence of CNR and FWHM on β for SQS-DBCN, SQS-noDB and SQS-PWLS at $\delta = 0.002/mm$. (a) and (c) MCs of nominal size 0.15-0.18 mm, (b) and (d) MCs of nominal size 0.18-0.25 mm. The SQS-DBCN, SQS-noDB, SQS-noNC CNR curves are the same as those in Fig. 5.

Fig. 14 shows the dependence of CNR and FWHM on β at $\delta = 0.002/mm$. The results of the SQS-PWLS method are very similar to those of the SQS-noDB method. The CNRs of the SQS-PWLS method are slightly lower than those of the SQS-noDB method, with a maximum difference of 5.3% for the 0.18-0.25 mm MCs at $\beta = 50$. The FWHM curves of SQS-PWLS and SQS-noDB overlap almost completely. We also examined the reconstructed image patches of the SQS-PWLS method. There is no visual difference between the images reconstructed by SQS-PWLS and SQS-noDB since a CNR difference of 5.3% is basically indistinguishable for human eyes. The similarity between those two methods is expected because we already demonstrated in the previous section that the spatial variation of σ_i^q within our studied conditions does not strongly affect the reconstructed image quality even in the worst case scenario. These results further justify the approximation of using constant noise variance in the SQS-DBCN method. The results also demonstrate that the MBIR method in CT that does not consider detector blur is not sufficient for DBT, where detector blur is one of the major image quality degrading factor.

X. Frequency Response of $\mathbf{S}_i$

As discussed in Section II.B of the paper, with the approximations of constant σ_i^q and σ_i^r for a given projection angle, we implemented $\mathbf{S}_i$ in the frequency domain with fast Fourier transform (FFT). Fig. 15 shows the normalized frequency response of $\mathbf{S}_i$ that corresponds to the central projection view of our experimental phantom. The specific frequency response of $\mathbf{S}_i$ will change based on the estimated σ_i^q and σ_i^r, which depend on the projection view angle. As a typical case, Fig. 15 shows that the high-frequency response of $\mathbf{S}_i$ is not extremely high such that noise of the projection views will not be amplified excessively.
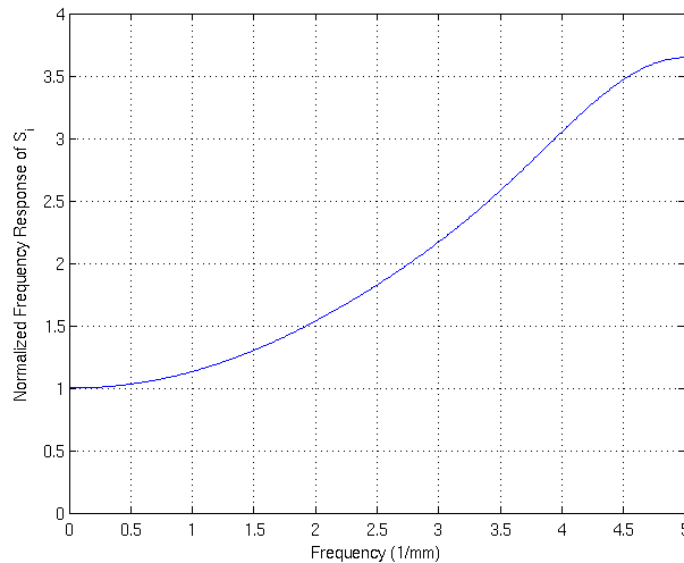

Fig. 15. Normalized frequency response of $\mathbf{S}_i$ for the central projection angle of the experimental phantom

XI. SQS-DBCN with Quadratic Regularization

In the implementation of the SQS-DBCN algorithm, we chose an edge-preserving regularization method by using the hyperbola potential function $\eta(t)$ (Equation (15)). $\eta(t)$ increases almost linearly when the

difference between neighboring pixels is large enough compared with δ; however, when δ is very large, the hyperbola potential function is approximately the quadratic function $\eta(t) = t^2$. We studied the performance of the SQS-DBCN algorithm with $\delta = 1/mm$, which represents a nearly quadratic regularizer. Fig. 16 shows the dependence of CNR of MCs on β. The peak of the curve moves to the lower-left corner when δ increases. When $\delta = 1/mm$, the peak CNR is only slightly higher than that of SART. The MC enhancement is much weaker when a quadratic regularization is used with the SQS-DBCN method. On a DBT slice, small MCs usually only occupy a few pixels. From the perspective of image processing, the entire MC may be processed as an 'edge' due to the high local gradient. So the MCs are strongly suppressed by a non-edge-preserving regularization. Fig. 17 and Fig. 18 show, respectively, examples of MCs in our phantom and soft tissue structures in human breast, such as a spiculated mass, reconstructed by SQS-DBCN with quadratic regularization for a range of β. The MCs are much more blurred than those by SQS-DBCN with hyperbola regularization as shown in Fig. 17, especially when β is large, so that small β is preferred for MCs. For soft tissue structures in human breast, SQS-DBCN with quadratic regularization produces texture that appears increasingly rough and "bumpy" when β decreases as shown in Fig. 18 so that large β is needed for more smooth and natural tissue texture. These results demonstrate that for quadratic regularization a single β cannot provide good image quality for both MCs and tissue texture or mass margin, which is crucial for DBT reconstruction.

The proposed SQS-DBCN model with hyperbola regularization is superior to that with quadratic regularization for DBT reconstruction as shown by our analyses. This can be explained by the dual roles played by the hyperbola potential function $\eta(t) = \delta^2\left(\sqrt{1 + (t/\delta)^2} - 1\right)$. For reconstructing soft tissue, the difference between neighboring pixels is small such that $\delta = 0.002/mm$ is large enough for the potential function to work in the 'quadratic' part of the curve. It therefore behaves like quadratic regularization that produces smooth and natural soft tissue texture at large β. For MCs with high gradient between neighboring pixels, the potential function behaves like linear regularization such that MCs are preserved even when relatively strong regularization is used to reduce noise. The property of the hyperbola function thus matches well with the requirements for DBT reconstruction.
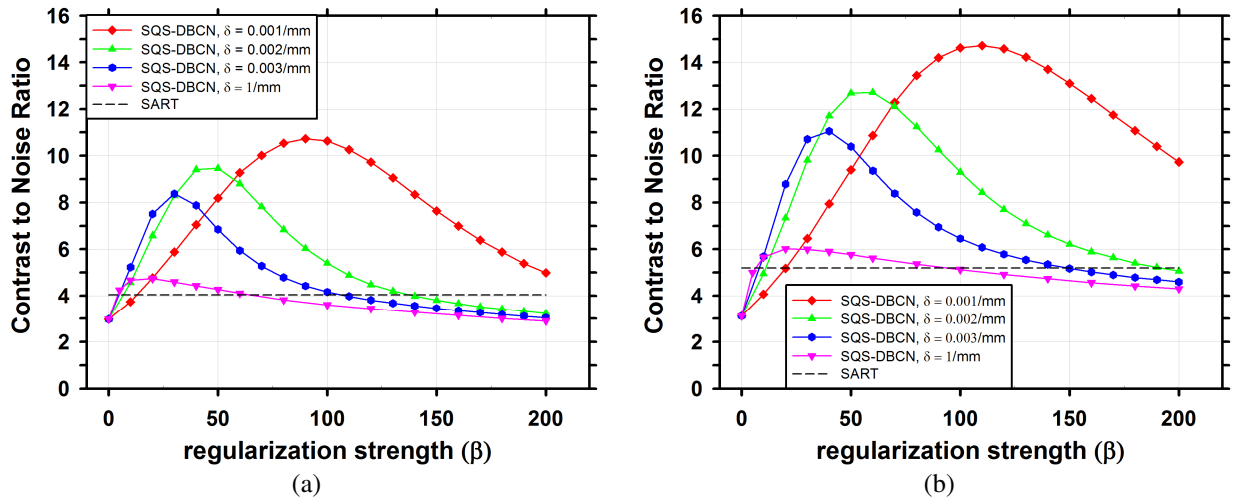

Fig. 16. Dependence of CNR on reconstruction parameters. (a) MCs of nominal size 0.15-0.18mm, (b) MCs of nominal size 0.18-0.25mm. These plots are the same as Fig. 2 with the addition of $\delta = 1/mm$ to approximate quadratic regularization.
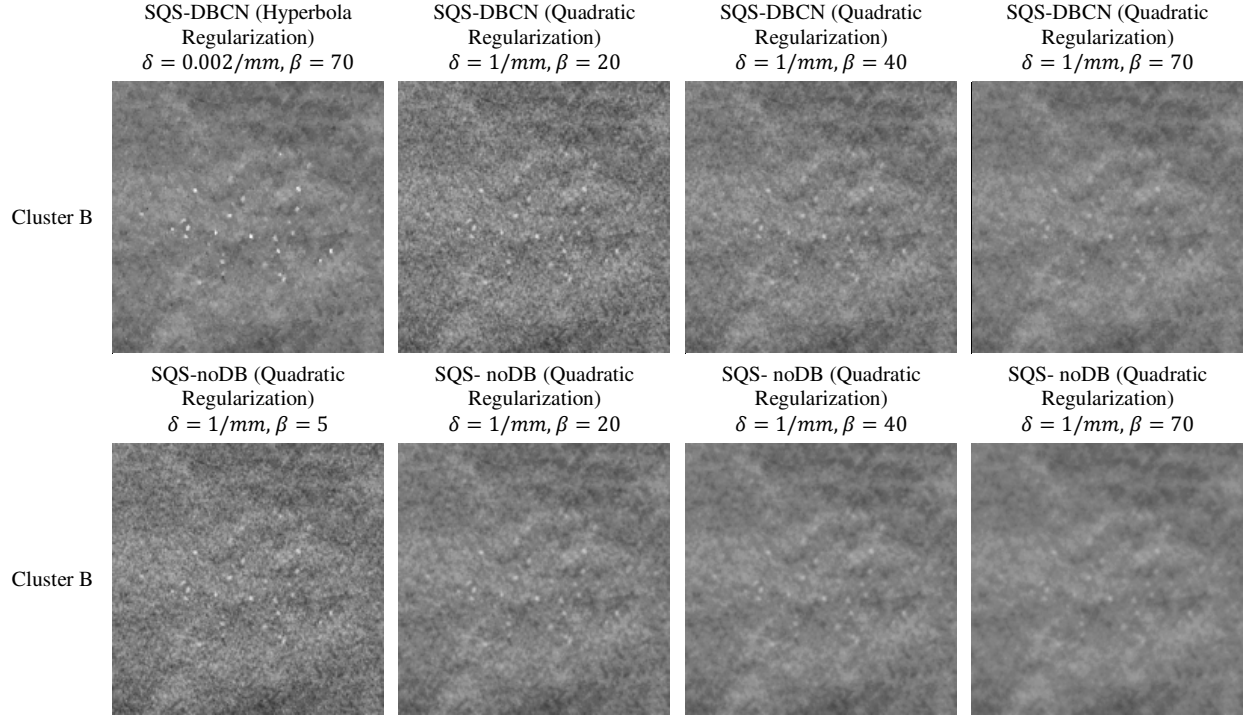
|SQS-DBCN (Hyperbola Regularization) $\delta = 0.002/mm, \beta = 70$ | SQS-DBCN (Quadratic Regularization) $\delta = 1/mm, \beta = 20$ | SQS-DBCN (Quadratic Regularization) $\delta = 1/mm, \beta = 40$ | SQS-DBCN (Quadratic Regularization) $\delta = 1/mm, \beta = 70$ |

Cluster B

|SQS-noDB (Quadratic Regularization) $\delta = 1/mm, \beta = 5$ | SQS- noDB (Quadratic Regularization) $\delta = 1/mm, \beta = 20$ | SQS- noDB (Quadratic Regularization) $\delta = 1/mm, \beta = 40$ | SQS- noDB (Quadratic Regularization) $\delta = 1/mm, \beta = 70$ |

Cluster B

Fig. 17. Comparison of MC clusters reconstructed with different reconstruction conditions. The SQS methods (SQS-DBCN or SQS-noDB) use 10 iterations. The images are displayed with the same window width setting.

|SQS-DBCN (Hyperbola Regularization) $\delta = 0.002/mm, \beta = 70$ | SQS-DBCN (Quadratic Regularization) $\delta = 1/mm, \beta = 20$ | SQS-DBCN (Quadratic Regularization) $\delta = 1/mm, \beta = 40$ | SQS-DBCN (Quadratic Regularization) $\delta = 1/mm, \beta = 70$ |
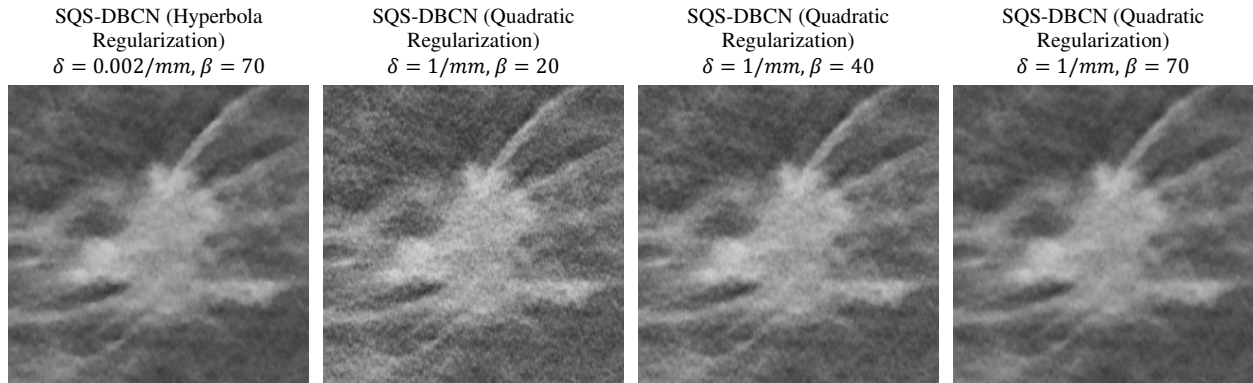
Fig. 18. Comparison of spiculated mass in human subject DBT. The images are displayed with the same window width setting.

We have shown in the paper (Fig. 5 to Fig. 9) the comparison of the SQS-DBCN model to that without modeling detector blur, i.e., SQS-noDB (Equation (30)), when the same hyperbola regularization was used. To further demonstrate the contribution of detector blur modeling, independent of the edge-preserving hyperbola regularizer, we compare the SQS-DBCN model and the SQS-noDB model, both with quadratic regularization, i.e., by setting $\delta = 1/mm$. Fig. 19 shows the CNR of MCs as a function of β. With or without modeling detector blur, the CNR curve reaches its peak value at small β. The SQS-noDB curves reaches its peak at smaller β, making it even more difficult to find a good trade-off to enhance the MCs while preserving the texture of soft tissue. Fig. 17 shows examples of MCs

reconstructed with the SQS-DBCN model and the SQS-noDB model using quadratic regularization for a range of β values. For a given β, the MCs by the SQS-noDB model are much more blurred and have lower contrast than that by the SQS-DBCN model, indicating that the proposed detector blur modeling improves both the image sharpness and the CNR values. This experiment shows that the advantages of detector blur modeling persist until β becomes very small regardless of whether edge-preserving regularization is used.
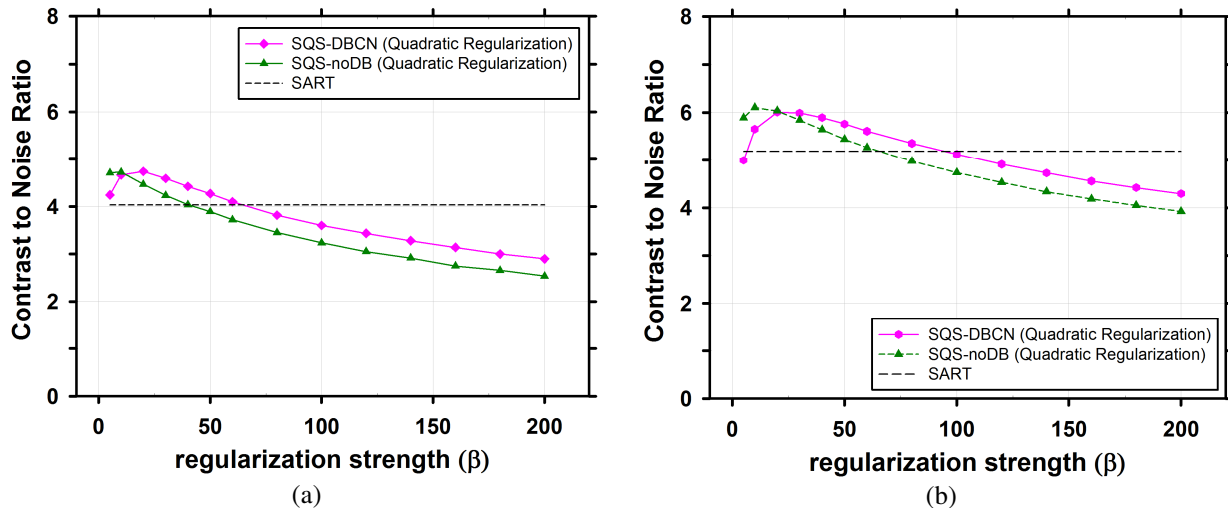
Fig. 19. CNR of MCs of the SQS-DBCN method and the SQS-noDB method when the quadratic regularization is used ($\delta = 1/mm$). (a) MCs of nominal size 0.15-0.18mm, (b) MCs of nominal size 0.18-0.25mm.

XII. Comparing SART and SQS-DBCN with the ACR Phantom and a Uniform Lucite Phantom

In addition to the breast phantom with heterogeneous background, we also compared the reconstruction methods using the ACR phantom. The results are shown in Fig. 20 and Fig. 21. Fig. 21 shows the third speck group on the ACR phantom. The visibility of the MCs is enhanced with the SQS-DBCN method, as indicated by the increased mean CNR of the six MCs.

We also compared the noise pattern in DBT slices of a uniform background reconstructed by the SART and the SQS-DBCN method. DBT scan of a 2-inch-thick uniform Lucite slab (about 5 cm) was acquired and reconstructed with the two methods. Fig. 22 shows noise patches from a slice at a depth of 2.7 cm in the Lucite phantom reconstructed by SART and the SQS-DBCN ($\delta = 0.002$, $\beta = 70$). Fig. 23 compares the noise power spectra obtained from averaging the noise power spectra of multiple noise patches at the same depth as the noise patches shown in Fig. 22 for each method. The SQS-DBCN method smooths the high-frequency noise but the low frequency noise is stronger compared to the SART method. The SQS-DBCN method does not generate obvious artifacts on the background with the parameters selected in our study.
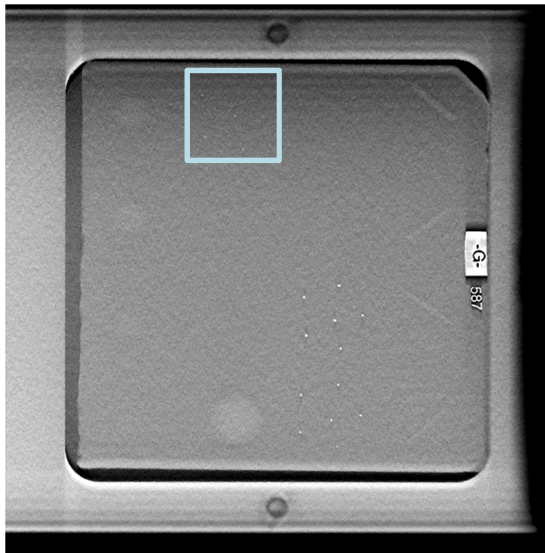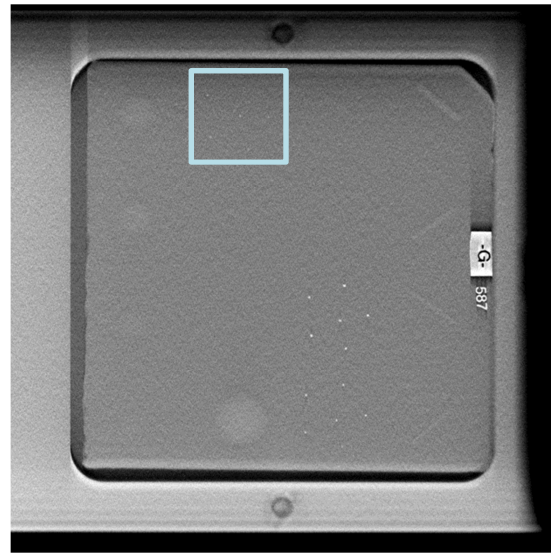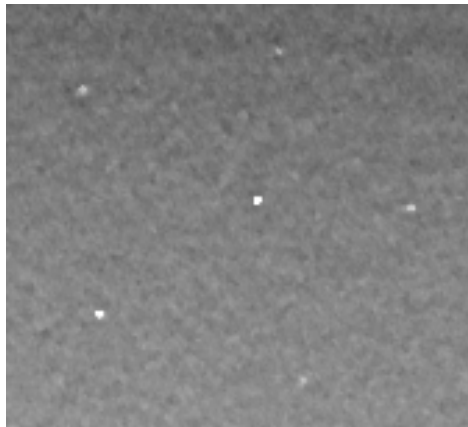
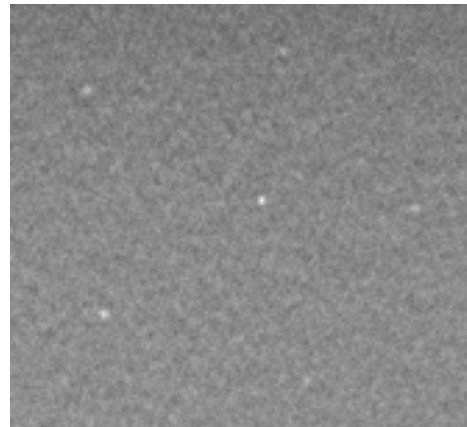(a) SQS-DBCN   (b) SART

Fig. 20. Comparison of reconstructed ACR phantom images. The images are displayed with the same window width setting. Fig. 21 shows a close-up view of the speck group marked by the box shown in Fig. 20. The x-ray source moves along the vertical direction. The horizontal artifacts on top and at the bottom of the images are caused by the rectangular block shape of the ACR phantom that results in an abrupt transition to air at the edge of the phantom. This artifact does not happen in a real breast and is different from the truncation artifacts caused by the finite field-of-view coverage by the detector. The stronger enhancement of SQS-DBCN compared to SART also causes stronger enhancement of the artifact.

(a) SQS-DBCN   (b) SART
(CNR = 17.5, FWHM = 0.33 mm)   (CNR = 7.07, FWHM = 0.38 mm)

Fig. 21. MC patches of reconstructed ACR phantom. The images are displayed with the same window width setting.
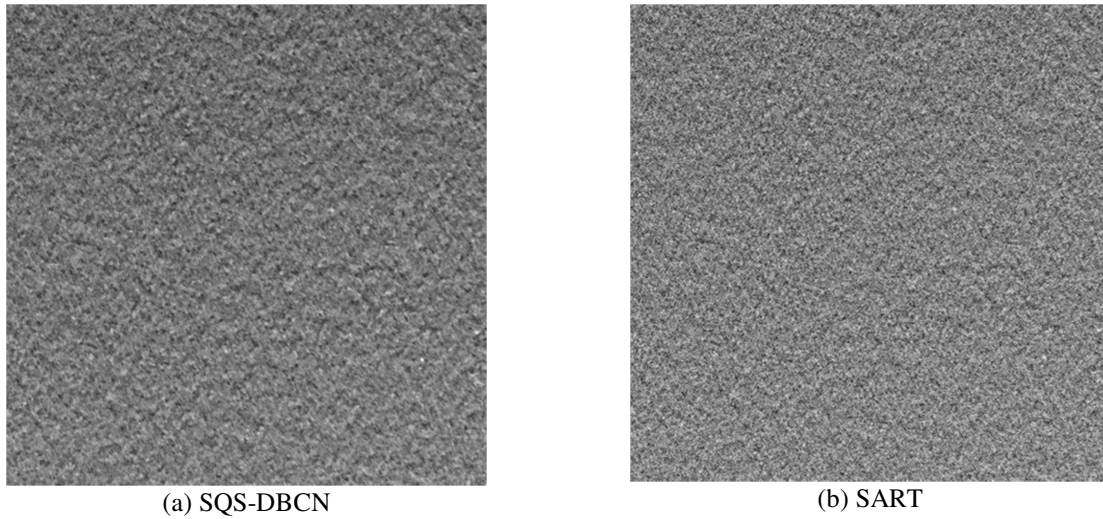
(a) SQS-DBCN

(b) SART

Fig. 22. Comparison of noise patches from a DBT slice of a uniform Lucite phantom reconstructed by SQS-DBCN ($\delta = 0.002$, $\beta = 70$) and SART. Both image patches are obtained from the same location in the two reconstructed DBT volume and the size of is 400×400 pixels (40×40 mm^2). The images are displayed with the same window width setting.
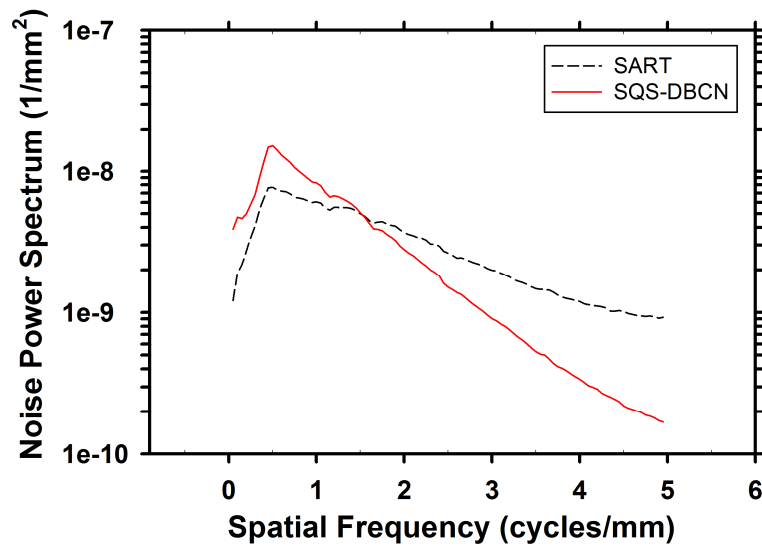

Fig. 23. Comparison of noise power spectra of noise patterns for the DBT slice of a uniform Lucite phantom reconstructed by SQS-DBCN ($\delta = 0.002$, $\beta = 70$) and SART at the same depth of the noise patches shown in Fig. 22.

REFERENCES

[50] B. De Man, S. Basu, N. Chandra, B. Dunham, P. Edic, M. Iatrou, S. McOlash, P. Sainath, C. Shaughnessy, B. Tower *et al.*, "Catsim : a new computer assisted tomography simulation environment," *Proc. SPIE,* vol. 6510, pp. U1191-U1198, 2007.

[51] B. De Man, J. Pack, P. FitzGerald, and M. Wu, *CatSim Manual Version 6.0*: GE Global Research, 2015.